論文 / 著書情報
Article / Book Information

Title(English)	Organic superconductors with an incommensurate anion structure
Authors(English)	Tadashi Kawamoto, Kazuo Takimiya
Citation(English)	Sci. Technol. Adv. Mater., Volume 10, Number 2, Page 024303
Pub. date	2009, 7
URL	http://www.iop.org/EJ/abstract/1468-6996/10/2/024303/
Creative Commons	See next page.

License

IOP PUBLISHING SCIENCE AND TECHNOLOGY OF ADVANCED MATERIALS

Sci. Technol. Adv. Mater. **10** (2009) 024303 (18pp) doi:10.1088/1468-6996/10/2/024303

TOPICAL REVIEW

Organic superconductors with an incommensurate anion structure

Tadashi Kawamoto[1] **and Kazuo Takimiya**[2]

[1] Department of Organic and Polymeric Materials, Graduate School of Science and Engineering, Tokyo Institute of Technology, O-okayama, Meguro-ku, Tokyo 152-8552, Japan
[2] Department of Applied Chemistry, Graduate School of Engineering, Hiroshima University, Kagamiyama, Higashi-Hiroshima, Hiroshima 739-8527, Japan

E-mail: kawamoto@o.cc.titech.ac.jp and ktakimi@hiroshima-u.ac.jp

Received 30 September 2008
Accepted for publication 26 January 2009
Published 6 July 2009
Online at stacks.iop.org/STAM/10/024303

Abstract

Superconducting incommensurate organic composite crystals based on the methylenedithio-tetraselenafulvalene (MDT-TSF) series donors, where the energy band filling deviates from the usual 3/4-filled, are reviewed. The incommensurate anion potential reconstructs the Fermi surface for both (MDT-TSF)$(AuI_2)_{0.436}$ and (MDT-ST)$(I_3)_{0.417}$ neither by the fundamental anion periodicity $\boldsymbol{q}$ nor by $2\boldsymbol{q}$, but by $3\boldsymbol{q}$, where MDT-ST is 5*H*-2-(1,3-dithiol-2-ylidene)-1,3-diselena-4,6-dithiapentalene, and $\boldsymbol{q}$ is the reciprocal lattice vector of the anion lattice. The *selection rule* of the reconstructing vectors is associated with the magnitude of the incommensurate potential. The considerably large interlayer transfer integral and three-dimensional superconducting properties are due to the direct donor–donor interactions coming from the characteristic corrugated conducting sheet structure.
The materials with high superconducting transition temperature, T_c, have large ratios of the observed cyclotron masses to the bare ones, which indicates that the strength of the many-body effect is the major determinant of T_c. (MDT-TS)$(AuI_2)_{0.441}$ shows a metal–insulator transition at $T_{MI} = 50$ K, where MDT-TS is 5*H*-2-(1,3-diselenol-2-ylidene)-1,3,4,6-tetrathiapentalene, and the insulating phase is an antiferromagnet with a high Néel temperature ($T_N = 50$ K) and a high spin–flop field ($B_{sf} = 6.9$ T). There is a possibility that this material is an *incommensurate Mott insulator*. Hydrostatic pressure suppresses the insulating state and induces superconductivity at $T_c = 3.2$ K above 1.05 GPa, where T_c rises to the maximum, $T_c^{max} = 4.9$ K at 1.27 GPa. This compound shows a usual temperature–pressure phase diagram, in which the superconducting phase borders on the antiferromagnetic insulating phase, despite the unusual band filling.

Keywords: organic superconductor, incommensurate composite crystal, Fermi surface, metal-insulator transition

(Some figures in this article are in colour only in the electronic version)

1. Introduction

In many organic superconductors, the ratio of the donor molecules to the anions is represented by an integer, typically D_2A (D = donor molecule, A = anion) [1–3]. The band filling of these compounds is 3/4, and this corresponds to effective half-filling in the presence of the dimerization gap. The donor–anion ratio takes a definite number for a given combination of donor and anion, and the ratio is constant; this differs from that in many inorganic compounds such as high-T_c cuprate superconductors, in which the ground state is determined by the carrier number. The ground states of organic compounds are regulated using the bandwidth by means of, for example, pressure.

Several groups have attempted to control the degree of charge transfer, i.e. band filling of organic conductors. The first method of controlling the charge transfer degree in organic conductors involves introducing composite anions of X^- and Y^{2-}, for example, $GaCl_4^-$ and $CoCl_4^{2-}$, respectively; this type of conductor changes from a band insulator to a metallic conductor, but does not show superconductivity [4–6]. Yamamoto and Kato [7] have used another approach; they have obtained several materials with unusual donor/anion ratios by mixing neutral molecules with the anions. They have not obtained a superconductor either. The use of noninteger composition, i.e. DA_x ($x \neq m/n$, $m, n = 1, 2, 3, \ldots$) is the third way, and compounds of this type include superconductors. Although there are many organic compounds with noninteger composition [8], this type of compound showing superconductivity is very limited. In the 1980s, the appearance of a superconducting phase was reported in the incommensurate crystals κ-$(ET)_4Hg_{2.78}Cl_8$ [9] and κ-$(ET)_4Hg_{2.89}Br_8$ [10], where ET is bis(ethylenedithio)tetrathiafulvalene. In the beginning of the 21st century, another organic superconductor with noninteger composition (MDT-TSF)$(AuI_2)_{0.436}$ was developed, where MDT-TSF is methylenedithio-tetraselenafulvalene [11].

Although there are many structurally incommensurate crystals they are classified into several categories, modulated structures, incommensurate composite crystals and quasi-crystals [12, 13]. An incommensurate charge–density–wave system and the high-T_c superconductor $Bi_2Sr_2CaCu_2O_{8+\delta}$ are in the category of modulated structures, and κ-$(ET)_4Hg_{3-\delta}X_8$ ($X = $ Br, Cl) and $Hg_{3-\delta}AsF_6$ are incommensurate composite crystals. In this article, we define an *incommensurate organic conductor* as an incommensurate composite crystal based on two interpenetrating lattice periodic structures that are mutually incommensurate. In general, we can describe the relation between the two real space lattices as

$$\begin{pmatrix} a' \\ b' \\ c' \end{pmatrix} = \boldsymbol{\sigma} \begin{pmatrix} a \\ b \\ c \end{pmatrix}, \tag{1}$$

where $\boldsymbol{\sigma}$ is an interlattice 3×3 matrix relating the real space translations of the sublattices [14]. For the simplest case, when both the b- and c-axes are common for both lattices and the a'-axis is parallel to the a-axis, the matrix elements of $\boldsymbol{\sigma}$, σ_{ij} $(i, j = 1, 2, 3)$, are expressed as

$$\boldsymbol{\sigma} = \begin{pmatrix} \sigma_{11} & 0 & 0 \\ 0 & 1 & 0 \\ 0 & 0 & 1 \end{pmatrix}. \tag{2}$$

In the case of $\sigma_{11} \neq m/n$ $(m, n = 1, 2, 3, \ldots)$ in equation (2), the crystal system is an *incommensurate* lattice structure.

An incommensurate composite crystal represents a single thermodynamic phase, and interactions between the subsystems are intrinsic to its existence, where the other subsystems act as incommensurate external potentials for the subsystem under consideration [13]. Therefore, an incommensurate organic conductor is interesting from the viewpoint of not only band filling but also aperiodic (or double periodic) ordered systems. In this article, we review the new incommensurate organic superconductors, the MDT-TSF series superconductors, from the sample preparation to the physical properties.

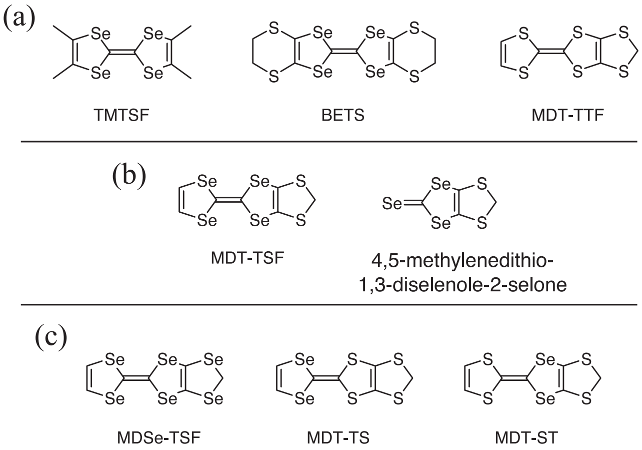

Figure 1. (a) Chemical structure of electron donors. (b) MDT-TSF (left) and its potential precursor (right). (c) Related electron donors of MDT-TSF.

2. Synthesis of MDT-TSF and its related donors and discovery of a series of superconductors

2.1. *Chemistry of TSF donors*

Before discussing the structural and physical aspects of the incommensurate superconductors based on MDT-TSF and its related donors in the following sections, we shall give a brief overview of the chemistry of the electron donors and how the present series of incommensurate superconductors were discovered. Until the latter half of the 1990s, the number and types of selenium variants of tetrathiafulvalene (TTF) were relatively limited [15]. This is mostly because of the lack of suitable synthesis methods and intermediates (in other words, building blocks); selenium reagents and selenium-containing starting materials are generally less accessible, more expensive and even more toxic in some cases than their corresponding sulfur reagents [16].

In the field of molecular conductors and superconductors, however, selenium-containing donors, particularly tetraselenafulvalene (TSF) derivatives, have played important roles; for example, the first molecular superconductors developed by Bechgaard *et al* [17] were based on TMTSF [tetramethyltetraselenafulvalene (figure 1(a))], and the unusual interplay between magnetic anions and conducting donor layers based on BETS [bis(ethylenedithio)tetraselenafulvalene (figure 1(a))] resulted in intriguing ‘magnetic superconductors’ [18]. Note that the TTF counterparts of these TSFs are known as electron donors capable of affording superconductors. In this regard, it is important to transform the TTF framework in the TTF-type donors yielding interesting conducting and/or superconducting

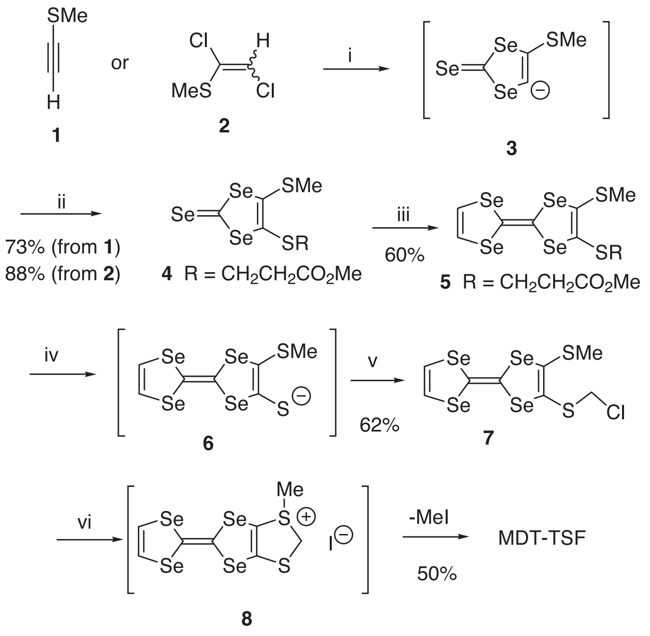

Reagents: (i) BuLi, Se, CSe$_2$, THF; (ii) NCS(CH$_2$)$_2$CO$_2$Me; (iii) 1,3-diselenole-2-selone, P(OMe)$_3$, Benzene; (iv) CsOH•H$_2$O (v) ClCH$_2$I; (vi) NaI, 2-butanone.

Figure 2. Synthesis of MDT-TSF.

radical cation salts into the TSF framework. One such molecular framework that remained unreachable was MDT-TTF [methylenedithio-tetrathiafulvalene (figure 1(a))] with a rather simple asymmetric electron donor framework, which was reported to afford a κ-type superconducting AuI$_2$ salt with T_c of 4.1–4.3 K [19, 20].

2.2. Synthesis of MDT-TSF

The major reason for the difficulty in the synthesis of the TSF variant of MDT-TTF, i.e. MDT-TSF, as shown in figure 1(b), is the fact that no method can be used to synthesize its direct precursor, 4,5-methylenedithio-1, 3-diselenole-2-chalcogenone. Although the successful synthesis of 4,5-methylenedithio-1,3-diselenole-2-selone (figure 1(b)) was achieved using one-pot synthesis of 1,3-diselenone-2-selone followed by direct annulation of the methylenedithio moiety in 1999 [21], it turned out that all the attempts of phosphite-mediated coupling reaction of the precursor have failed. This forced us to devise another synthesis method capable of affording the methylenedithio-annulated TSF derivatives. After several trials, the synthesis strategy thus developed was the initial formation of the TSF skeleton followed by the construction of the methylenedithio moiety, as shown in figure 2 [11].

This route involves a combination of effective synthesis techniques newly developed, namely, one-pot formation of 1,3-diselenole-2-selone from a terminal alkyne [22], a trialkyl phosphite-mediated coupling reaction to the TSF derivative, and finally heterocycle formation by transalkylation on a chalcogen atom [23]. In addition, a deprotection/realkylation protocol of a protected TSF-thiolate building block **5** was newly established for this synthesis [24]. For the first step, methylthioacetylene (**1**) [25] or 1,2-dichloro-1-methylthioethane (**2**) [26] was successively treated with nBuLi, selenium powder, and carbon diselenide, to generate *in situ* the vinyl anion intermediate (**3**), which was then quenched with 3-thiocyanatopropionic acid methyl ester [27] to give a 1,3-diselenole-2-selone derivative (**4**) in 73 or 88% yield. Cross-coupling of **4** with unsubstituted 1,3-diselenole-2-selone gave the desired asymmetrical TSF derivative **5** in 60% yield. Treatment of **5** with cesium hydroxide monohydrate in *N,N*-dimethylformamide (DMF) generated the reactive TSF monothiolate (**6**), which was alkylated *in situ* with chloroiodomethane to give **7** in 62% isolated yield. Formation of the outer 1,3-dithiolene ring was achieved by an initial halogen exchange to the corresponding iodide followed by spontaneous transalkylation into MDT-TSF via the sulfonium salt **8**.

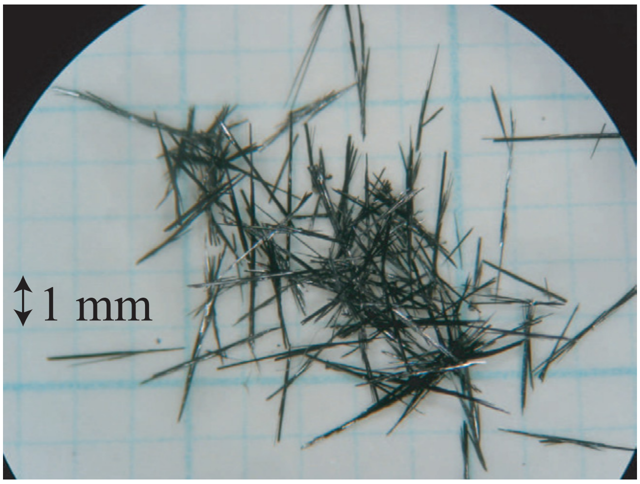

Figure 3. Needlelike crystals of (MDT-TSF)(AuI$_2$)$_{0.436}$.

2.3. AuI$_2$ salt of MDT-TSF

Because MDT-TTF gave the superconducting AuI$_2$ salt, electrocrystallization of MDT-TSF in the presence of tetrabutylammonium diiodoaurate as a supporting electrolyte in chlorobenzene was first examined. Within a few days, needle-shaped crystals (figure 3) were obtained: note that κ-(MDT-TTF)$_2$AuI$_2$ was reported to be platelike crystals. Its electrical conductivity measured along the needle direction was very high (2000 S cm^{-1}, an average of 8 samples) at room temperature. Resistivity decreases with decreasing temperature and abruptly drops at 4.5 K, which is characteristic of the onset of a superconducting transition (figure 4). The magnetization with a superconducting quantum interference device (SQUID) magnetometer also reveals its superconductivity (figure 5). The diamagnetic shielding at 2 K shows 80% of the perfect diamagnetism, indicating that the salt is a bulk superconductor. In both zero-field-cooled (ZFC) and field-cooled (FC) measurements, the magnetization starts to decrease at 4.2 K, which is slightly lower than the value obtained in the resistivity measurement.

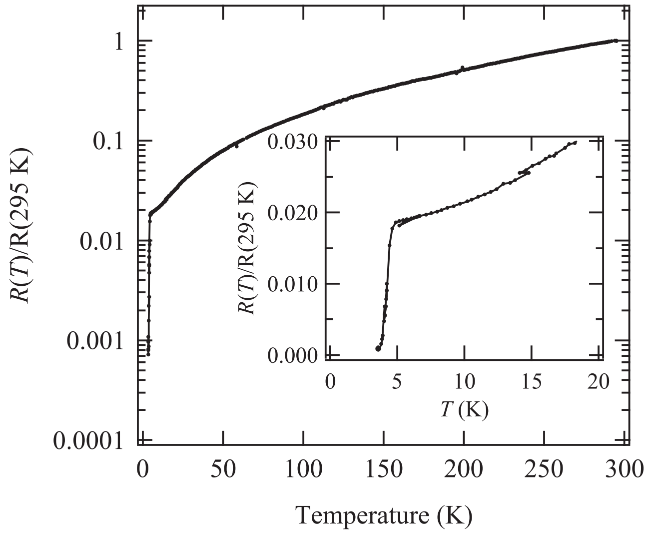

Figure 4. Temperature dependence of resistivity of (MDT-TSF)$(AuI_2)_{0.436}$.

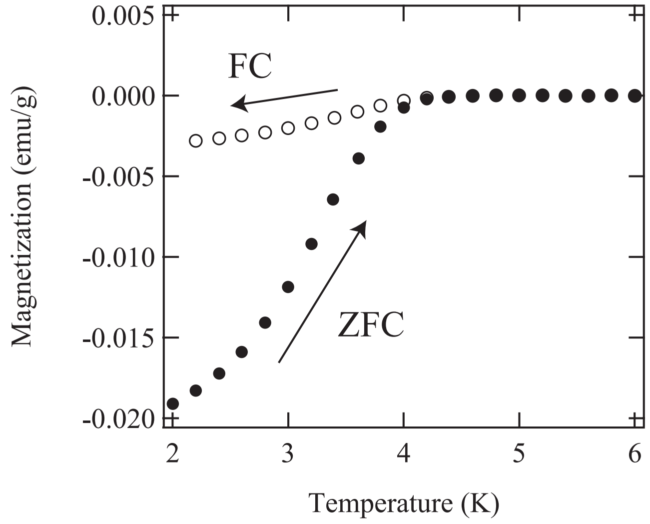

Figure 5. Temperature dependence of the magnetization of (MDT-TSF)$(AuI_2)_{0.436}$ at an applied field of 5 Oe. Filled circles represent zero-field-cooled (ZFC) data and open circles represent field-cooled (FC) data.

2.4. *MDT-TSF radical salts with other linear anions*

As will be mentioned in the following sections in detail, the characteristic features that differentiate the present MDT-TSF-AuI_2 from 'ordinary' molecular superconductors are twofold, i.e. its crystal and electronic structures. In sharp contrast to the conventional molecular superconductors with dimeric donor structure, MDT-TSF-AuI_2 consists of *uniform* donor stacks. Furthermore, the periodicity of the donor stacks is different from that of the anion lattice, resulting in an *incommensurate* structure with a noninteger donor:anion ratio of 1 : 0.436 [for this reason the salt is expressed as (MDT-TSF)$(AuI_2)_{0.436}$]; this ratio is unique among molecular superconductors, where the conventional ratio is 2 : 1 [28].

For the development of such unique organic superconductors, it is important to determine whether the structural features of (MDT-TSF)$(AuI_2)_{0.436}$ are limited to this particular combination. From this standpoint, other MDT-TSF salts with various linear anions were synthesized, and it was found that combinations of MDT-TSF and trihalide anions such as I_3^- and I_2Br^- afford similar superconducting salts with incommensurate structures (figure 6 and table 1) [29].

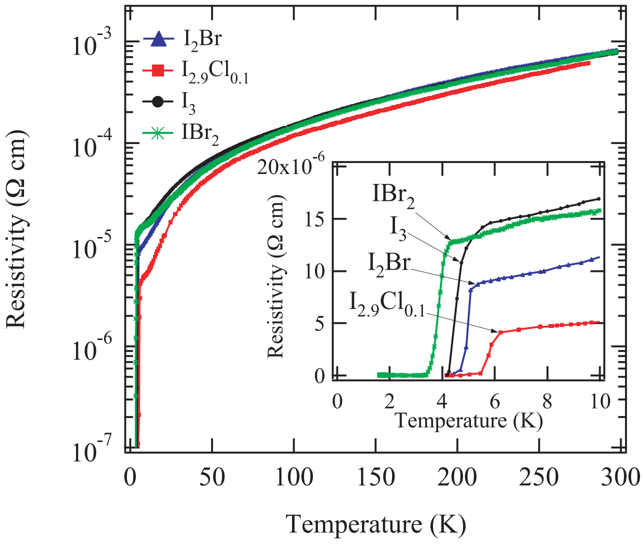

Figure 6. Temperature dependence of resistivity of trihalide salts of MDT-TSF. The materials are distinguished by the X part (I_3, I_2Br, IBr_2 and $I_{2.9}Cl_{0.1}$) of the supporting electrolyte $(n\text{-}Bu_4N)X$ used in the electrocrystallization.

2.5. *Related methylenedichalcogenotetrachalcogenafulvalenes*

It was unclear whether only MDT-TSF could allow the formation of such unique *incommensurate* superconductors or if related electron donors could also do so. In this regard, it was already reported that MDT-TTF, i.e. an all-sulfur analogue of MDT-TSF, yielded a superconducting AuI_2 salt, κ-(MDT-TTF)$_2$$AuI_2$ [19, 20], but its crystal and electronic structures differ from those of (MDT-TSF)$(AuI_2)_{0.436}$. In addition, an all-selenium analogue of MDT-TSF, namely, MDSe-TSF [methylenediseleno-tetraselenafulvalene, figure 1(c)] yielded a superconducting bromine salt with a T_c of 4 K [35], whereas its crystal structure was again classified as κ-type. The other related donors then focused on were two isomeric methylenedithio-diselenadithiafulvalenes [MDT-TS and MDT-ST, figure 1(c)].

Although MDT-TS has been known since 1988 when Papavassiliou *et al* [36] reported the donor in a conference proceedings, the isomeric donor MDT-ST has not been described at all. Taking advantage of new intermediate **4** and the synthesis methodologies developed for the synthesis of MDT-TSF, we successfully synthesized MDT-ST (figure 7(a)) [30]. By contrast, the reported procedure for the synthesis of MDT-TS was not reproducible, and thus, a modified synthesis of MDT-TS was examined, which gave better results (figure 7(b)) [31].

Electrocrystallizations of the donors with linear anions gave radical cation salts with the incommensurate anion structure (table 1). All three salts of MDT-ST were found to

Table 1. Chemical composition, room temperature conductivity σ_{rt}, charge transfer degree ρ and superconducting transition temperature T_c of the incommensurate superconductors based on MDT-TSF and its related donors [11, 28–34].

Donor	X^a	σ_{rt} (S cm^{-1})^b	Chemical composition^c	ρ(e)	T_c (K)^e
MDT-TSF	AuI_2	2000	$(MDT\text{-}TSF)(AuI_2)_{0.436}$	0.436	4.5 (4.2)
	I_3	1500	$(MDT\text{-}TSF)(I_3)_{0.422}$	0.422	4.9 (4.4)
	I_2Br	1500	$(MDT\text{-}TSF)I_{1.19}Br_{0.08}$	0.42^d	5.0 (4.8)
	IBr_2	1300	$(MDT\text{-}TSF)I_{0.77}Br_{0.52}$	0.43^d	4.0 (4.4)
	$I_{2.9}Cl_{0.1}$	1500	$(MDT\text{-}TSF)I_{1.27-\delta}Cl_\delta$ ($\delta \sim 0$)	0.42^d	5.5 (5.0)
MDT-ST	I_3	600–1200	$(MDT\text{-}ST)(I_3)_{0.417}$	0.417	3.6^f(3.8)
	I_2Br	400 ± 200	$(MDT\text{-}ST)I_{1.27-\delta}Br_\delta$ ($\delta \sim 0.2$)	0.42^d	3.2 (3.8)
	$I_{2.9}Cl_{0.1}$	300 ± 200	$(MDT\text{-}ST)I_{1.27-\delta}Cl_\delta$ ($\delta \sim 0$)	0.41^d	3.4 (4.0)
MDT-TS	AuI_2	600	$(MDT\text{-}TS)(AuI_2)_{0.441}$	0.441	4.0^g

[a] The supporting electrolyte $(n\text{-}Bu_4N)X$ has been used in the electrocrystallization.

[b] Measured on a single crystal by a four-probe method along the a-axis.

[c] The chemical composition was determined on the basis of the x-ray oscillation photograph and the elemental analysis as described in the text.

[d] The degree of charge transfer was estimated assuming that the trihalide anion is the charged species.

[e] The midpoint of resistivity drop is defined as T_c in the resistivity measurement, and the onset of diamagnetic transition in the magnetization measurements with a SQUID magnetometer is in parentheses.

[f] The high-quality samples show $T_c = 4.3$ K in the resistivity measurements [33].

[g] The superconducting transition appears only under high pressure. The present value is the midpoint T_c (onset $T_c = 4.7$ K) under $P = 1.14$ GPa [31, 34].

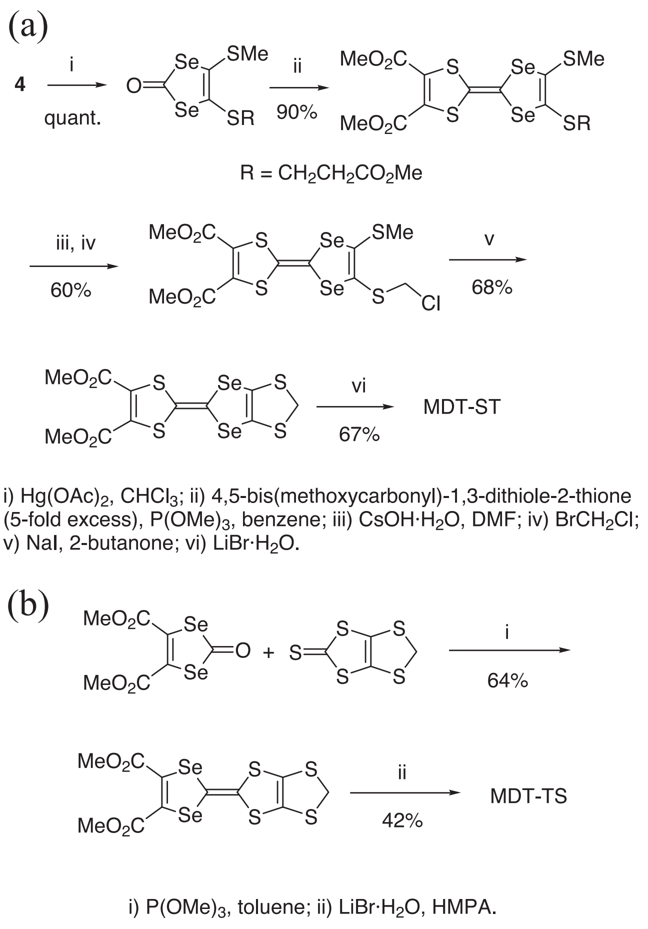

i) $Hg(OAc)_2$, $CHCl_3$; ii) 4,5-bis(methoxycarbonyl)-1,3-dithiole-2-thione (5-fold excess), $P(OMe)_3$, benzene; iii) $CsOH{\cdot}H_2O$, DMF; iv) $BrCH_2Cl$; v) NaI, 2-butanone; vi) $LiBr{\cdot}H_2O$.

i) $P(OMe)_3$, toluene; ii) $LiBr{\cdot}H_2O$, HMPA.

Figure 7. Syntheses of (a) MDT-ST and (b) MDT-TS.

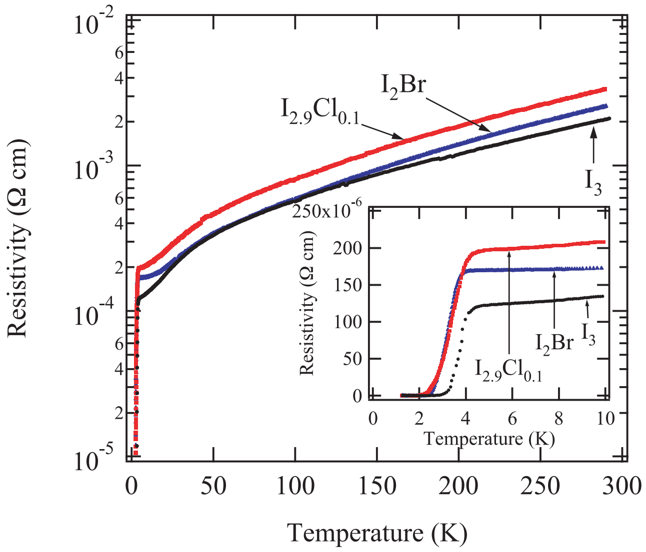

Figure 8. Temperature dependence of resistivity of MDT-ST salts. The materials are distinguished by the X part (I_3, I_2Br and $I_{2.9}Cl_{0.1}$) of the supporting electrolyte $(n\text{-}Bu_4N)X$ used in the electrocrystallization.

be superconducting under ambient pressure with T_c values slightly lower than those of MDT-TSF salts (figure 8) [30], whereas the conducting behavior of the AuI_2 salt of MDT-TS was strikingly different from those of the other salts listed in table 1; the salt showed a resistivity minimum at $T_\rho = 85$ K and metal–insulator transition at $T_{MI} = 50$ K. Application of hydrostatic pressure (1.14 GPa), on the other hand, induced a superconducting transition at the onset $T_c = 4.7$ K (midpoint $T_c = 4.0$ K; see section 5 for details) [31, 34].

The difference in the conducting behavior of the MDT-TS salts from those of the MDT-TSF and MDT-ST salts can be explained by considering that the intermolecular overlaps in the MDT-TS salt are insufficient to retain the metallic state to low temperature. In particular, the intermolecular overlaps between the donor stacks depend on the position of selenium atoms, as can be seen from the general molecular arrangement in the bc plane (figure 9); it is highly likely

Table 2. Experimentally determined charge transfer degrees ρ, superconducting transition temperatures T_c and lattice parameters [11, 28–33, 37].

Material	ρ(e)	T_c (K)	a(Å)	b(Å)	c(Å)	V(Å^3)
(MDT-TSF)(AuI$_2$)$_{0.436}$	0.436	4.5	4.016(6)	12.513(3)	25.424(3)	1277(1)
(MDT-TSF)(I$_3$)$_{0.422}$	0.422	4.9	4.013(4)	12.539(2)	25.620(2)	1289(1)
(MDT-ST)(I$_3$)$_{0.417}$	0.417	4.3	3.961(1)	12.361(2)	25.392(5)	1243.2(4)
(MDT-TS)(AuI$_2$)$_{0.441}$	0.441	4.9[a]	3.993(5)	12.448(4)	25.115(5)	1248(1)

[a] The present value is the maximum midpoint T_c under hydrostatic pressure, $P = 1.27$ GPa [37].

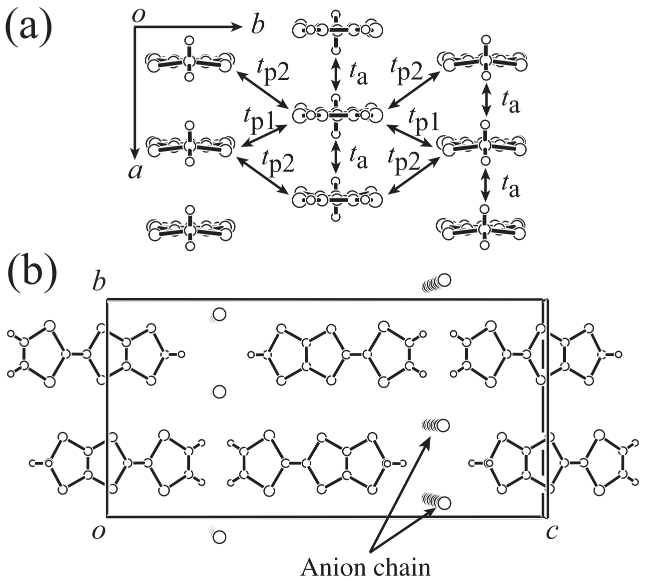

Figure 9. General molecular arrangement in the incommensurate superconductors based on MDT-TSF, MDT-ST and MDT-TS. (a) Crystal structure projected along the molecular long axis and (b) projection onto the bc plane. Note that the inter-stack interaction through the central 1,3-dichalcogenole rings is most effective.

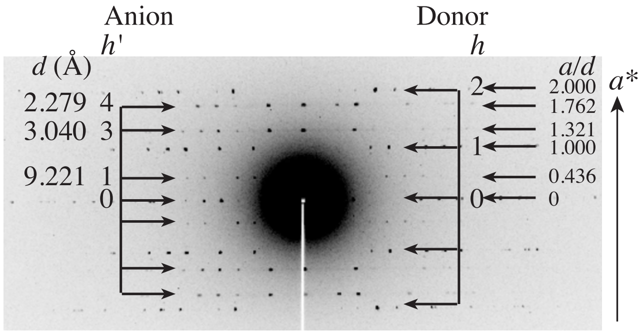

Figure 10. X-ray oscillation photograph of (MDT-TSF)(AuI$_2$)$_{0.436}$ along the a^*-axis at room temperature.

that the introduction of selenium atoms in the central 1,3-dichalcogenole ring is crucial for stabilizing the metallic state.

2.6. Summary

With the successful synthesis of MDT-TSF and the discovery of the first superconducting AuI$_2$ salt as a starting point, a series of organic superconductors with an incommensurate anion lattice based on MDT-TSF and its related donors have been discovered. The present series of ‘incommensurate’ superconductors may raise several intriguing points that should be addressed, including the effects of incommensurate anion potential on the donor lattice, T_c depending on the degree of charge transfer, and chemical pressure effects caused by different chalcogene atoms in the same molecular framework. Some of these will be discussed in the following sections.

3. Incommensurate lattice and charge transfer degree

The x-ray crystal structure analysis of the AuI$_2$ salt of the MDT-TSF has been performed [11]. The space group is $Pnma$, and the lattice parameters are listed in table 2. The AuI$_2$ salt has a uniform donor stacking with a head-to-head mode along the a-axis, and there is no disorder (figure 9(a)). The donors form a conducting sheet on the ab plane. It is characteristic of this crystal structure that, in contrast to other layered organic superconductors, the donor molecules form a corrugated sheet structure with direct donor–donor interactions along the c-axis (figure 9(b)). Although the linear anion AuI$_2^-$ runs along the a-axis, the length of the a-axis is shorter than that of the AuI$_2^-$ [11]. These structural features are common to all MDT-TSF series conductors with linear anions.

Figure 10 is an x-ray oscillation photograph of (MDT-TSF)(AuI$_2$)$_{0.436}$, in which the vertical direction is parallel to the donor stacking axis (a^*-axis) [28]. This photograph shows clear incommensurate layer lines at $a/d = 0.436$, 1.321 and 1.762 reciprocal lattice units based on the donor subcell. All these layer lines are composed of well-defined spots even at room temperature, indicating the three-dimensional order of the anion molecules. The layer lines at $a/d = 0.436$, 1.321 and 1.762 respectively correspond to $h' = 1$, 3 and 4 lines of the subcell constant $a' = 9.221$ Å. Hereafter, we represent the donor and anion lattices as indices h and h', respectively. The lattice constant of the anion cell is in agreement with the length of the AuI$_2^-$ anion. The $h' = 2$ line is not clearly observed despite the clear $h' = 3$ line, because the latter ($d = 3.04$ Å) comes from the average bond length of Au–I. The clear spots at $h' = 1$ indicate that the anion structure is not a random infinite chain composed of Au and I, but has a discrete unit of I–Au–I.

We consider that the b and c axes are common to both the donor and anion lattices. The ratio of a to a' unambiguously determines the AuI$_2$ content to be $x = a/a' = 0.436$, namely, (MDT-TSF)(AuI$_2$)$_{0.436}$. The present compound has the same interlattice matrix as that expressed in equation (2) with $1/\sigma_{11} = 0.436$. This composition is consistent with the results of both energy dispersion spectroscopy (1 : 0.434) and elemental analysis (1 : 0.44). Although the closest integer ratio of donor to anion is 9 : 4 (1 : 0.444), this seems to exceed the error of the x-ray investigation. Therefore, we have to conclude an incommensurate composition, (MDT-TSF)$(AuI_2)_{0.436}$ on the basis of these three experiments.

The MDT-TSF series superconductors presented in this review have the same interlattice matrix type as that expressed in equation (2), in which only the diagonal elements of $\boldsymbol{\sigma}$ are not zero. By contrast, the interlattice matrix of κ-$(ET)_4Hg_{2.89}Br_8$ is defined as the translation from the lattice of ET and Br to the lattice of Hg [38]. The matrix is not as simple as that of the MDT-TSF series salts, i.e. $\sigma_{12} = \sigma_{21} = \sigma_{23} = \sigma_{31} = \sigma_{32} = 0$.

The x-ray oscillation photograph of (MDT-TSF)$(I_3)_{0.422}$ does not show the $h' = 1$ line, indicating that the I_3^- unit is not definite [29]. It is well known that iodide exists in the forms of I^-, I_2, I_3^- and I_5^- in solids, and the Raman spectrum can be used to determine the state of iodide [39]. Figure 11(a) shows the Raman spectra of (MDT-TSF)$(I_3)_{0.422}$ at room temperature [32]. The a-parallel spectrum consists of the 104 cm^{-1} peak and its overtones, which is known as the symmetric stretching mode of I_3^- in an infinite linear chain [39, 40]. This demonstrates that the anion is a polyiodide chain composed of I_3^- units, which differs from a discrete I_3^-. By contrast, the b-parallel spectrum shows no Raman line originating from the iodide anion. These observations indicate the existence of the iodide chain running along the a-axis.

For (MDT-ST)$(I_3)_{0.417}$, the $h' = 2$ line of the I_3^- anion lattice has been observed in the x-ray oscillation photograph [33]. The interlattice matrix is the diagonal type with $1/\sigma_{11} = 0.417$ and $\sigma_{22} = \sigma_{33} = 1$. The a-parallel Raman spectrum of this salt also shows the symmetric stretching mode of I_3^- in an infinite linear chain [33].

The obtained charge transfer degree of (MDT-TSF)$(I_3)_{0.422}$, $\rho = 0.422$, is slightly smaller than that of (MDT-TSF)$(AuI_2)_{0.436}$. This is explained on the basis of the crystal structure and anion length. The a-axis of the donor lattice of the I_3 salt, 4.013(4) Å, is almost the same as that of the AuI_2 salt, 4.016(6) Å, and the length of I_3^- ($a' = 9.507$ Å) is greater than that of AuI_2^- ($a' = 9.221$ Å); this is in agreement with the usual relationship of the anion length between AuI_2^- and I_3^- [1]. Consequently, the anion content, 0.422, determined from a/a' is smaller than that of (MDT-TSF)$(AuI_2)_{0.436}$.

The Raman spectrum is sensitive to the charge on the organic donor or acceptor molecules. The ring C = C stretching mode, which is the C = C stretching mode along the molecular short axis, is Raman-active for the MDT-TSF molecule because of the symmetry of the molecular structure. The neutral MDT-TTF molecule with the same symmetry as MDT-TSF exhibits two strong Raman lines at 1510 and 1551 cm^{-1}; the first line is assigned to the ring C = C bond [41]. This Raman line shifts to 1470 cm^{-1} for κ-(MDT-TTF)$_2$AuI$_2$. This indicates that the Raman shift decreases by approximately 40 cm^{-1} for a 0.5 charge transfer degree. The Raman line at 1499 cm^{-1} labeled as ν_1 in the neutral MDT-TSF, which linearly decreases as the charge transfer degree ρ increases, corresponds to the ring C = C bond, and is related to the degree of charge transfer as $\nu_1 = 1499 - 67.63\rho$, as shown in figures 11(b) and (c) [32]. Although the linewidths of the present Raman spectra are considerably broad, the shift of ν_1 is regarded as the second piece of evidence of the difference in the degree of charge transfer between the AuI_2 and I_3 salts.

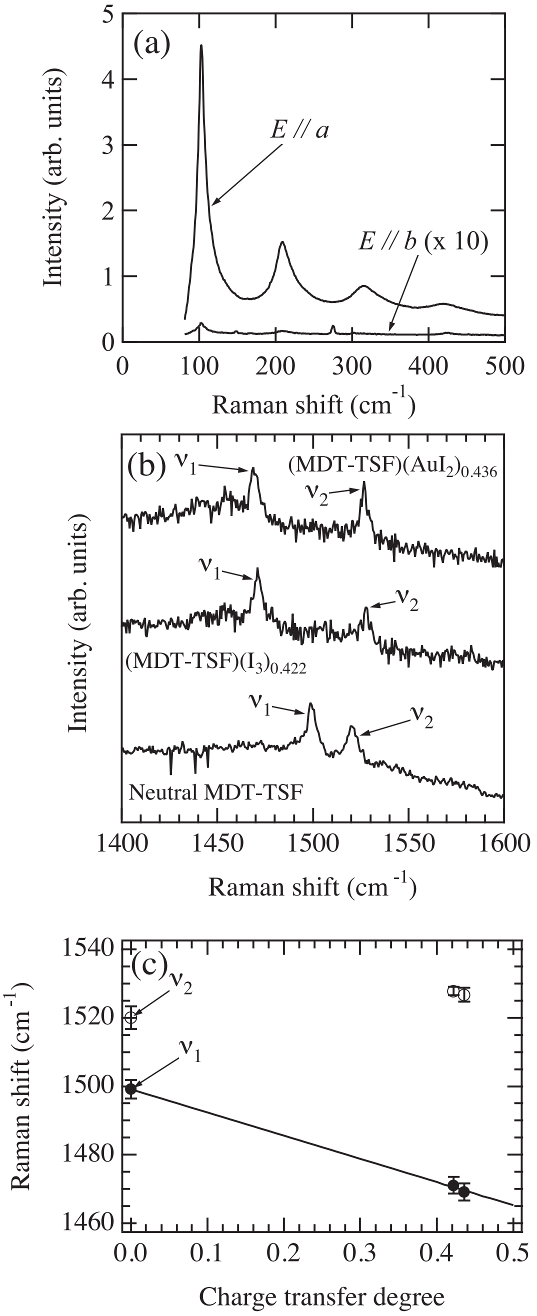

Figure 11. (a) Raman spectra of (MDT-TSF)$(I_3)_{0.422}$ and (b) Raman spectra of MDT-TSF salts and neutral MDT-TSF. (c) Charge-transfer degree dependence of the Raman shifts of MDT-TSF salts.

Table 3. Calculated transfer integrals and the cross-sectional area of the fundamental closed orbits, γ and δ orbits, based on the room temperature atomic coordinates [32–34, 48].

Material	t_a (meV)	t_{p1} (meV)	t_{p2} (meV)	$A_{F,\gamma}/A_{\mathrm{BZ}}$ (%)	$A_{F,\delta}/A_{\mathrm{BZ}}$ (%)
$(\text{MDT-TSF})(\text{AuI}_2)_{0.436}$	106.9	−10.3	−35.4	8.5	43.6
$(\text{MDT-TSF})(\text{I}_3)_{0.422}$	123.5	−6.6	−37.5	9.1	42.2
$(\text{MDT-ST})(\text{I}_3)_{0.417}$	103.8	−8.8	−34.1	7.7	41.7
$(\text{MDT-TS})(\text{AuI}_2)_{0.441}$	76.0	−7.9	−26.3	8.3	44.1

In addition to the I_3 salt, I_xBr_y salts have been obtained (table 1). The ratio between iodide and bromine differs from the original composition, I_2Br and IBr_2; therefore, the anions are in a disordered state. However, all MDT-TSF, MDT-ST and MDT-TS salts with I_xBr_y show superconductivity despite the disordered anions [29, 30].

4. Electronic states of the ambient pressure superconductors: MDT-TSF salts and MDT-ST salts

4.1. Energy band calculation

The energy band calculation including an incommensurate anion potential is very complicated because of the use of superspace, and the band structures of only two incommensurate organic conductors, $(\text{BO})_{2.4}\text{I}_3$ [42], where BO is bis(ethylenedioxy)tetrathiafulvalene, and $(\text{ET})\text{Hg}_{0.776}(\text{SCN})_2$ [43], have been calculated. The incommensurate potential effect on the Fermi surface depends on the materials in these calculations. Although small gaps open at the Fermi surface for $(\text{BO})_{2.4}\text{I}_3$, the Fermi surface disappears in a large area for $(\text{ET})\text{Hg}_{0.776}(\text{SCN})_2$.

The energy band structure has been calculated on the basis of the atomic coordinates of the donor molecules in the donor cell without the anion lattice potential using the extended Hückel method and the tight binding approximation [44]. The atomic orbital parameter set of Se strongly affects the results of the calculations [45]. The parameter set tuned to BETS salts [46] without both 3d orbitals of S and 4d orbitals of Se has turned out to be suitable for the MDT-TSF series conductors [32, 47–49]. The transfer integrals, t_i, are estimated from the intermolecular overlap integrals S_i as $t_i = E \times S_i$, in which the energy level of the highest occupied molecular orbital E is taken to be $-10\,\text{eV}$. The interaction modes (a, p1 and p2) are defined in figure 9(a).

The calculated transfer integrals are shown in table 3, and the energy band structure and Fermi surface of $(\text{MDT-TSF})(\text{AuI}_2)_{0.436}$ are shown in figure 12. The energy bands are degenerated on the C line of the zone boundary owing to the donor lattice symmetry ($Pnma$) [50]. Therefore, the Fermi surface is composed of the overlapping cylinders, and there are two fundamental γ and δ orbits. The cross-sectional area ratios between the fundamental Fermi surface and the first Brillouin zone, $A_{\mathrm{F}}/A_{\mathrm{BZ}}$, are also shown in table 3. Although the γ pocket area depends on the transfer integrals ratio, the δ orbit area is equal to the degree of charge transfer and is independent of the transfer integral values.

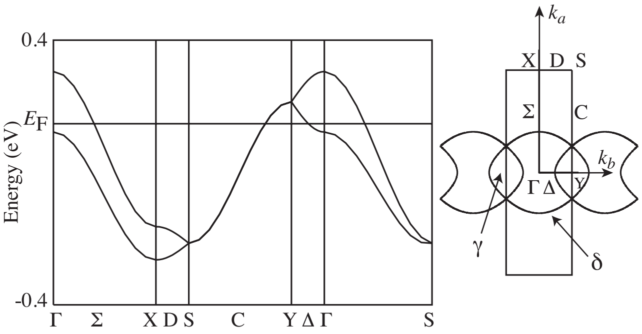

Figure 12. Energy band structure and Fermi surface of $(\text{MDT-TSF})(\text{AuI}_2)_{0.436}$.

The polarized optical reflectance is a useful tool for estimating the band parameters for organic conductors [51]. The plasma frequencies obtained from the optical reflectance spectra of $(\text{MDT-TSF})(\text{AuI}_2)_{0.436}$ are $\omega_{p,a} = 0.88\,\text{eV}$ for the a-axis and $\omega_{p,b} = 0.55\,\text{eV}$ for the b-axis [48]. The α-direction plasma frequency is calculated using the following equation derived from the Boltzmann equation [51]:

$$\omega_{p,\alpha}^2 = \frac{ne^2}{\epsilon_0\hbar^2}\,\frac{\int\int\int \frac{\partial^2 E(k)}{\partial k_\alpha^2} f(E(k))\mathrm{d}k_a\mathrm{d}k_b\mathrm{d}k_c}{\int\int\int f(E(k))\mathrm{d}k_a\mathrm{d}k_b\mathrm{d}k_c}, \qquad (3)$$

where n is the carrier number density, e is the elementary electric charge, ϵ_0 is the vacuum permittivity, $\hbar$ is the Plank constant, $E(k)$ is the energy dispersion and $f(E(k))$ is the Fermi–Dirac distribution function. The calculated values of $\omega_{p,a} = 0.85\,\text{eV}$ and $\omega_{p,b} = 0.61\,\text{eV}$ are in good agreement with the experimental estimation. Thus, we have adopted the method to calculate the band structure based on the x-ray crystal structure analysis of the donor lattice.

4.2. Incommensurate anion potential effect on the Fermi surface

For many years, the Fermi surface topologies of metals and organic conductors have been studied using techniques such as the de Haas–van Alphen and Shubnikov–de Haas oscillations [3, 52, 53]. In this respect, the Fermi surface under a superlattice structure is of interest because when a superlattice potential is added to the original lattice, the Brillouin zone is reconstructed in accordance with the new reciprocal lattice. If the periodicity of the superlattice potential is *commensurate* with the original one, it is easy to define the new Brillouin zone; for instance, the original Brillouin zone is simply halved along the $\boldsymbol{a}^*$-axis of the reciprocal

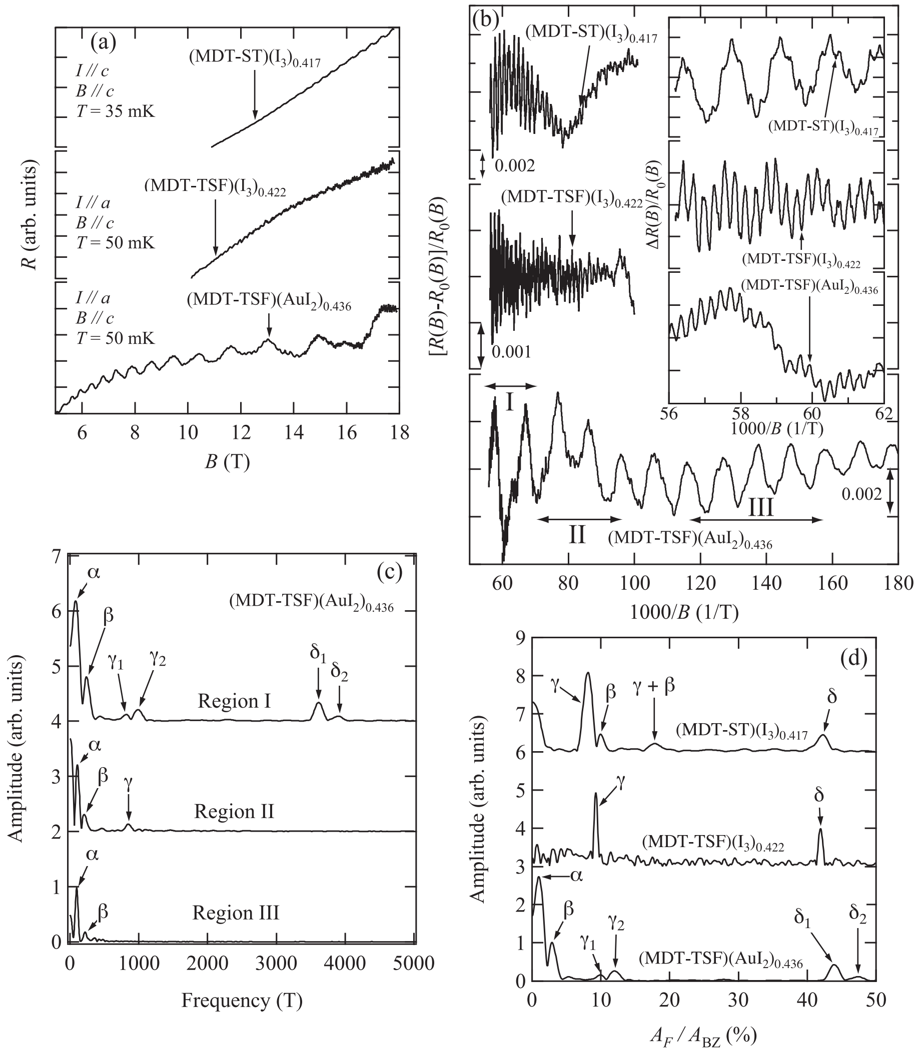

Figure 13. (a) Magnetoresistances of (MDT-TSF)$(AuI_2)_{0.436}$, (MDT-TSF)$(I_3)_{0.422}$, and (MDT-ST)$(I_3)_{0.417}$. (b) Shubnikov–de Haas signals. The inset is the high field region. (c) Fast Fourier transformation spectra of the Shubnikov–de Haas oscillations of (MDT-TSF)$(AuI_2)_{0.436}$ in the field regions I–III defined in (b). (d) Fast Fourier transformation spectra of the Shubnikov–de Haas oscillations in (MDT-TSF)$(AuI_2)_{0.436}$, (MDT-TSF)$(I_3)_{0.422}$ and (MDT-ST)$(I_3)_{0.417}$.

lattice if the superlattice vector $\boldsymbol{q}$ is $\boldsymbol{a}^*/2$. However, when the $\boldsymbol{q}$ vector is *incommensurate*, we cannot generally define the Brillouin zone. Azbel first dealt with this problem within the generalized Kronig–Penny model, and pointed out that the incommensurate periodic potential is a natural intermediate between periodicity and randomness [54]. It creates a devil's stair-type energy spectrum, and then one may expect fine structures in the quantum oscillations.

An incommensurate potential as a modulated structure is introduced on electronic states by density wave formation in various materials. In η-Mo_4O_{11} [55] and $NbSe_3$ [56], for instance, the electronic states are subject to the incommensurate superlattice potential by the charge-density-wave formation. In these materials, the Shubnikov–de Haas oscillations with very low frequencies have been observed below the charge-density-wave transition temperature, which can be ascribed to small closed orbits formed by the Fermi surface reconstruction using the fundamental periodic vector $\boldsymbol{q}$ of the charge-density-wave. In the case of incommensurate composite crystals, $Hg_{3-\delta}AsF_6$ and $Hg_{3-\delta}SbF_6$, the results of the de Haas–van Alphen measurements have also been explained on the basis of the Fermi surface reconstruction using the fundamental periodic vector $\boldsymbol{q} = a^*(\delta, \pm\delta, 0)$ of the incommensurate mercury-chain sublattice [57, 58]. The validity of such simple zone-folding procedures, which have been empirically adopted to explain the experimental results in many cases, is not trivial because the obtained energy bands do not meet the translational symmetry of the superlattice or sublattice.

An incommensurate potential effect on the Fermi surface has been investigated using the Shubnikov–de Haas oscillation measurements of the MDT-TSF series superconductors, because the above problem has not been discussed in detail. The Shubnikov–de Haas oscillation of (MDT-TSF)$(AuI_2)_{0.436}$ is shown in figure 13(a) [47]. The oscillatory part (Shubnikov-de Haas signal) of the resistance is represented by $[R(B) - R_0(B)]/R_0(B)$, rescaled using the nonoscillatory background $R_0(B)$ (figure 13(b)). Figure 13(c) shows the fast Fourier transformation spectra obtained in various field regions defined as I–III in figure 13(b). The

Table 4. Shubnikov–de Haas frequencies, cross-sectional Fermi surface area ratios, effective cyclotron masses and the Dingle temperatures [32, 47, 49].

Material	F_{expt} (T)	$A_{\mathrm{F}}/A_{\mathrm{BZ}}(\%)$	m^*/m_0	$T_{\mathrm{D}}(\mathrm{K})$
(MDT-TSF)$(\mathrm{AuI_2})_{0.436}$	100 (α)	1.2	0.6	0.1
	210 (β)	2.5	1.1	1.0
	820 (γ_1)	9.9	–[a]	–[a]
	860 (γ)	10.4	2.8	0.3
	990 (γ_2)	12.0	–[a]	–[a]
	3600 (δ_1)	43.7	3.9	1.9
	3900 (δ_2)	47.3	4.8	1.7
(MDT-TSF)$(\mathrm{I_3})_{0.422}$	764 (γ)	9.3	4.1	0.5
	3450 (δ)	42.0	5.1	1.3
(MDT-ST)$(\mathrm{I_3})_{0.417}$	704 (γ)	8.1	1.7	2.4
	816 (β)	9.4	2.1	4.0
	1540 ($\gamma+\beta$)	17.8	2.2	4.1
	3660 (δ)	42.3	2.9	4.4

[a] The effective cyclotron mass of the γ orbit is the average of the γ_1 and γ_2 orbits, because we could not separate this in two peaks in some measurements.

fast Fourier transformation spectra show six closed orbits, α, β, γ_1, γ_2, δ_1 and δ_2. The angular dependence of the Shubnikov–de Haas frequencies indicates that the Fermi surfaces are cylindrical. The Shubnikov–de Haas signals have been analyzed conventionally using the Lifshitz–Kosevich formula. The obtained Shubnikov–de Haas parameters are summarized in table 4.

The band calculation based on the donor arrangement gives overlapping cylindrical Fermi surfaces (figure 12), in which the cross section of the large cylinder is 43.6%, and the small overlapping area is approximately 8.5% of the first Brillouin zone. The observed cross section of the δ_1 orbit, $A_{\mathrm{F},\delta_1}/A_{\mathrm{BZ}} = 43.7\%$, is in agreement with the large cross section estimated from the band calculation. This number is also equal to the amount of charge transfer coming from the anion content of (MDT-TSF)$(\mathrm{AuI_2})_{0.436}$. The γ orbit is assigned to the 8.5% overlapping area. Although the energy bands are degenerated on the C line owing to the donor lattice symmetry, the incommensurate anion lattice along the a-axis may destroy this symmetry. This broken symmetry makes the δ_1 orbit a magnetic breakdown orbit that appears only at high fields.

In figure 13(c), two close Shubnikov–de Haas frequencies tend to appear as pairs, δ_1–δ_2 and γ_1–γ_2 coming from the interlayer transfer integral. From these pairs, the interlayer transfer integral is roughly estimated as $t_\perp \sim 2\,\mathrm{meV}$ under a parabolic energy band approximation, and the value is consistent with the results ($t_\perp = 1\,\mathrm{meV}$) of the analysis of the resistance peak structure under the magnetic field almost parallel to the conducting sheet in the angular magnetoresistance [48], which is explained on the basis of the Fermi surface warping [59]. The large $t_\perp$ is due to the direct donor–donor interactions coming from the corrugated conducting sheet structure (figure 9(b)).

Two low-frequency orbits, the α and β orbits, are not explained by the band calculation. This indicates that the incommensurate anion potential reconstructs the Fermi surface. The Fermi surface reconstruction using the fundamental anion periodicity $\boldsymbol{q} = 0.436\boldsymbol{a}^*$, $2\boldsymbol{q}$ and $3\boldsymbol{q}$ is shown in figure 14(a), where we assume the Fermi surface shape to be an ellipse with the overlapping area corresponding to the γ_1 orbit. Although the vector $\boldsymbol{q}$ does not make a new pocket, $2\boldsymbol{q}$ and $3\boldsymbol{q}$ lead to new overlapping regions. The $3\boldsymbol{q}$ vector makes two new pockets, which are approximately 3 and 0.3% of the first Brillouin zone. The former is assigned to the β orbit. Although the latter pocket does not exactly agree with the α orbit, the small pocket is considered to be sensitive to the reconstruction. Therefore, the α orbit can be assigned to this smallest pocket. The $2\boldsymbol{q}$ vector makes a new overlapping area of 25%, but this is too large to be interpreted as the observed α and β orbits. Then, the observed orbits are explained on the basis of the $3\boldsymbol{q}$ reconstruction of the Fermi surface.

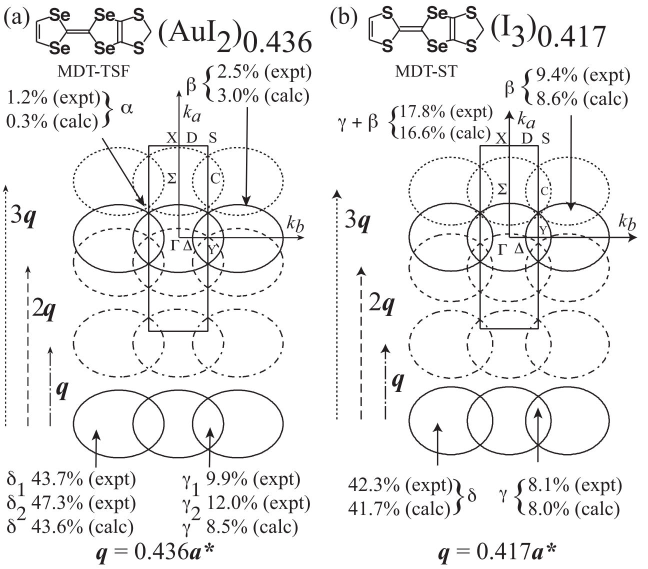

Figure 14. Fermi surfaces reconstructed using $\boldsymbol{q}$ (dash-dotted lines), $2\boldsymbol{q}$ (dashed lines), and $3\boldsymbol{q}$ (dotted lines) of (a) (MDT-TSF)$(\mathrm{AuI_2})_{0.436}$ and (b) (MDT-ST)$(\mathrm{I_3})_{0.417}$. The original Fermi surfaces (solid lines) are also represented in both panels. The first Brillouin zone is calculated from the donor cell. The calculated closed area of the $\mathrm{AuI_2}$ salt is based on the room temperature atomic coordinates, and that of the $\mathrm{I_3}$ salt is based on 18.5 K atomic coordinates.

In contrast to the mercury chain compounds explained on the basis of a simple $\boldsymbol{q}$ vector originating in the incommensurate mercury chain, the Fermi surface of the present compound is reconstructed by $3\boldsymbol{q}$. This characteristic reconstruction is related to the intensity of the anion sublattice reflections observed in the x-ray oscillation photograph. Although the spots of both $\boldsymbol{q}$ and $3\boldsymbol{q}$ are clearly observed, the $2\boldsymbol{q}$ spot is not found in the x-ray photograph (figure 10). This is associated with the absence of the $2\boldsymbol{q}$ reconstruction. The x-ray $3\boldsymbol{q}$ intensities are even stronger than the $\boldsymbol{q}$ intensities. The $\boldsymbol{q}$ vector comes from the fundamental repeating period of the AuI$_2$ anion, while the $3\boldsymbol{q}$ potential is strong because this is associated with the average distance of Au–I and I–I. The conduction electrons mainly feel the additional incommensurate potential generated by the interatomic distance of the AuI$_2$ chain.

The fine structure in the quantum oscillations predicted by Azbel has not been observed. The reason is probably as follows: the incommensurate potential is significantly smaller than that made by the donor molecules, and the conduction electrons perturbatively feel the incommensurate potential. In real materials, the magnitudes of various sublattice potentials are different, and only one or a few modulations are usually predominant. The predominant potential makes larger energy gaps in the original bands at the boundaries of the new Brillouin zone than the other higher-order sublattice potentials. In the Shubnikov–de Haas experiments, such small energy gaps formed by the higher-order potentials are not observable because of the magnetic breakdown. This scenario affords the *selection rule* of the reconstructing vectors. The *selection rule* is probably validated only when the incommensurate potential is treated perturbatively. The present system provides a very rare case in which the principal potential is not of the fundamental periodicity.

(MDT-ST)(I$_3$)$_{0.417}$ also has the Fermi surfaces reconstructed by the incommensurate anion potential [49]. The energy band calculation results cannot explain the β and $\gamma+\beta$ orbits in figure 13. The x-ray oscillation photograph of this compound shows that the intensity of the $3\boldsymbol{q}$ ($= 3 \times 0.417\boldsymbol{a}^*$) spots is even stronger than that of the other $n\boldsymbol{q}$ spots, where n is an integer [33]; the vector $3\boldsymbol{q}$ is associated with the average distance of I–I in the real space. The *selection rule* requires that the shift vector of the Fermi surface should be $3\boldsymbol{q}$. The observed orbits are explained on the basis of the $3\boldsymbol{q}$ reconstruction of the Fermi surface, as shown in figure 14(b). Although two new closed orbits, α and β, appear in the case of (MDT-TSF)(AuI$_2$)$_{0.436}$ (figure 14(a)), the α orbit vanishes and the β orbit area becomes larger (8.6% of the first Brillouin zone) than the γ orbit area in the case of (MDT-ST)(I$_3$)$_{0.417}$ (figure 14(b)), where we assume the Fermi surface shape of the δ orbit to be an ellipse with the overlapping area corresponding to the γ orbit. These results are closely associated with the difference in the charge transfer degree between (MDT-ST)(I$_3$)$_{0.417}$ and (MDT-TSF)(AuI$_2$)$_{0.436}$.

The Shubnikov–de Haas oscillations of (MDT-TSF)(I$_3$)$_{0.422}$ have also been measured, as shown in figure 13 [32]. The observed δ orbit is in agreement with the charge transfer from the anion content 0.422, and this value is the third piece of evidence that the charge transfer degree is slightly smaller than that of (MDT-TSF)(AuI$_2$)$_{0.436}$ as shown in figure 13(d). The *selection rule* requires that the Fermi surface is reconstructed by $3\boldsymbol{q} = 3 \times 0.422\boldsymbol{a}^*$ on the basis of the x-ray oscillation photograph, and the new closed orbit, β orbit with $F \sim 520\,\mathrm{T}$, should be observed. However, the fast Fourier transformation spectrum does not show such an extra orbit. This indicates that the interaction between the donor molecules and the incommensurate anion potential is extremely small, and the conduction electrons do not perturbatively feel the incommensurate potential.

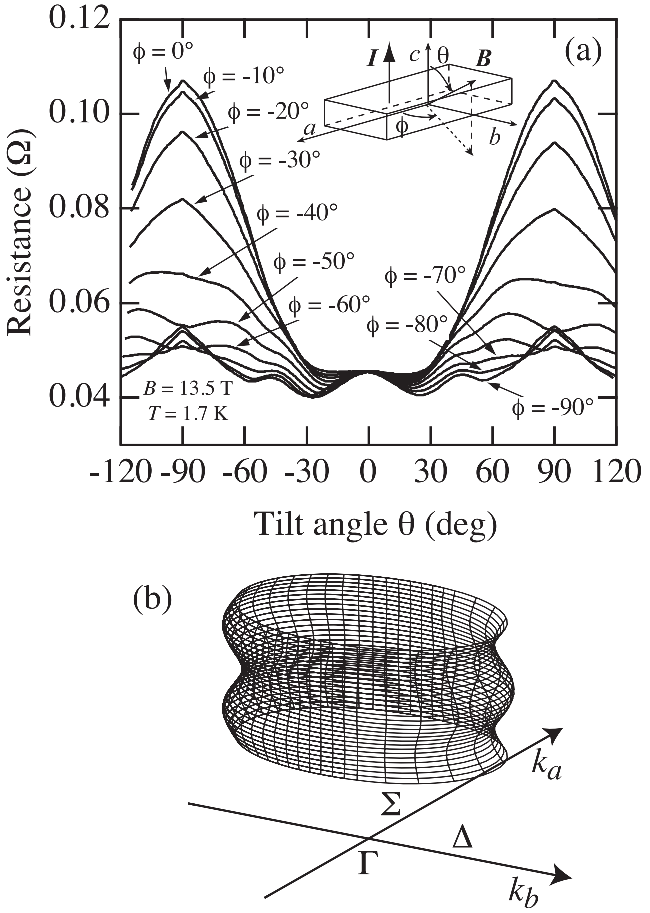

Figure 15. (a) Angular magnetoresistance oscillations of (MDT-ST)(I$_3$)$_{0.417}$. (b) p-type staggered warping Fermi surface. The magnitude of the k_c-axis warping has been increased to emphasize the corrugation shape.

4.3. Staggered warping Fermi surface of (MDT-ST)(I$_3$)$_{0.417}$

The angular magnetoresistance oscillation of (MDT-ST)(I$_3$)$_{0.417}$ is shown in figure 15(a) [49]. The field orientation is defined using a tilt angle θ and an azimuthal angle ϕ in the inset of figure 15(a). Although the usual shape of angular magnetoresistance oscillations has a minimum at $\theta = 0^\circ$ in a quasi-two-dimensional system, the present data have a broad peak at $\theta = 0^\circ$, whose magnitude increases with increasing $|\phi|$. This peak is not observed in (MDT-TSF)(AuI$_2$)$_{0.436}$ with similar Fermi surfaces [48].

Yagi and Iye have demonstrated that the $\theta = 0^\circ$ peak appears when the Fermi surface has p-type or d_{xy}-type staggered warping [60]. The angular magnetoresistance oscillation for p-type corrugation has a twofold symmetry with respect to the azimuthal angle ϕ, whereas d_{xy}-type corrugation gives a fourfold symmetrical angular magnetoresistance oscillation. Moreover, they have pointed out that the $\theta = 0°$ peak intensity decreases with decreasing $|\phi|$ for p-type corrugation. The observed angular magnetoresistance oscillation of the present compound in figure 15(a) meets the requirements of p-type corrugation. All Fermi surfaces are made on the basis of the zone folding of the single energy band corresponding to the δ orbit. Therefore, it is reasonable to assume that the energy band of the δ orbit has p-type energy dispersion. The energy dispersion relation of the corrugated cylindrical Fermi surface is generally

$$E = \frac{\hbar^2}{2m_a}k_a^2 + \frac{\hbar^2}{2m_b}k_b^2 - 2t_\perp(\phi)\cos(d_\perp k_\mathrm{c}), \tag{4}$$

where m_i is the effective mass along the k_i direction, $d_\perp$ is the effective interlayer spacing ($d_\perp = c/2 = 12.643(2)$ Å at 18.5 K [33]), and $t_\perp(\phi)$ is the interlayer transfer integral depending on the azimuthal angle ϕ. For p-type warping, $t_\perp(\phi)$ is described as

$$t_\perp(\phi) = t_\perp(k_a, k_b) = \frac{k_b}{\sqrt{k_a^2 + k_b^2}}t_\mathrm{c}, \tag{5}$$

where t_c is the constant transfer integral along the k_c direction [60]. This formula demonstrates that the interlayer transfer integral is zero on the Σ-line in the first Brillouin zone, as shown in figure 15(b), for the fundamental Fermi surface, the δ orbit. Therefore, the field inclination at $\phi = 0°$ is least affected by the p-type corrugation of the Fermi surface, and hence, the $\theta = 0°$ peak is minimized at this special ϕ. The $\theta = 0°$ peak is also observed for the high-T_c cuprate superconductor $\mathrm{Tl_2Ba_2CuO_{6+\delta}}$; the feature is explained in terms of a higher-order corrugation with a fourfold symmetry in the fundamental Fermi surface [61].

4.4. Superconductivity

The superconducting properties of (MDT-TSF)$(\mathrm{AuI_2})_{0.436}$, (MDT-TSF)$(\mathrm{I_3})_{0.422}$, and (MDT-ST)$(\mathrm{I_3})_{0.417}$ have been investigated using magnetoresistance measurements [28, 32, 62]. For example, the upper critical fields, B_{c2}, of (MDT-TSF)$(\mathrm{I_3})_{0.422}$ are shown in figure 16(a). The Ginzburg–Landau coherence lengths, $\xi_{\parallel a}$, $\xi_{\parallel b}$, and $\xi_{\parallel c}$, estimated from $B_{c2\parallel i}(T) = \Phi_0/[2\pi\xi_{\parallel j}(T)\xi_{\parallel k}(T)]$, where Φ_0 is the flux quantum, are listed in table 5. The in-plane coherence lengths, $\xi_{\parallel a}$ and $\xi_{\parallel b}$, are much shorter than the cyclotron radius of the δ-orbit (0.15 μm at 14 T for (MDT-TSF)$(\mathrm{I_3})_{0.422}$) estimated from the Shubnikov–de Haas oscillations. Therefore, these compounds are clean-limit superconductors. The transverse coherence length [$\xi_{\parallel c}$ as shown in figure 16(b)] is greater than the thickness of the conducting sheet $c/2 \sim 12.8$ Å, indicating that the superconductivity is three-dimensional (3D).

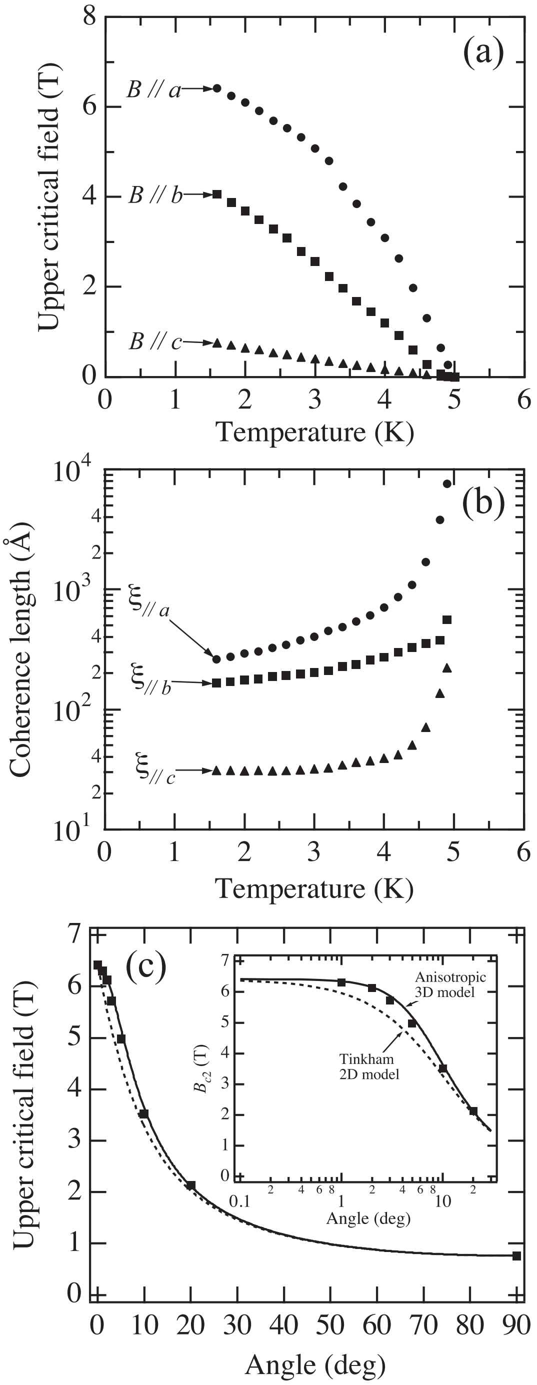

Figure 16. Temperature dependence of the (a) upper critical fields and (b) Ginzburg–Landau coherence lengths. (c) Angular dependence of the upper critical field. The solid and dotted lines represent the results of calculations based on the anisotropic 3D model and 2D model, respectively. The inset in (c) is the low-angle region. The material for all panels is (MDT-TSF)$(\mathrm{I_3})_{0.422}$.

The field angle dependence of the upper critical field depends on the superconducting dimensionality. For anisotropic 3D superconductors, the field angle dependence of the upper critical field is

$$\left(\frac{B_{c2}(\theta)\sin\theta}{B_{c2\perp}}\right)^2 + \left(\frac{B_{c2}(\theta)\cos\theta}{B_{c2\parallel}}\right)^2 = 1, \tag{6}$$

Table 5. Charge transfer degree ρ, superconducting transition temperature T_c, calculated density of states at the Fermi level $N(E_F)$, effective cyclotron mass ratio m^*/m_0, calculated cyclotron mass ratio m_c/m_0, ratio between the effective and calculated cyclotron masses m^*/m_c, and Ginzburg–Landau coherence length at 1.6 K ($\xi_{\parallel a}$, $\xi_{\parallel b}$, and $\xi_{\parallel c}$) [28, 32, 47, 49, 62]. The total density of states $N(E_F)$ is given in units of (total states) eV^{-1} (donor molecule) $^{-1}$.

Material	ρ (e)	T_c(K)	$N(E_F)$	m^*/m_0	m_c/m_0	m^*/m_c
	$\xi_{\parallel a}$(Å)	$\xi_{\parallel b}$(Å)	$\xi_{\parallel c}$(Å)			
(MDT-TSF)$(I_3)_{0.422}$	0.422	4.9	1.93	4.1 (γ)	2.2	1.9
	261	166	31	5.1 (δ)	3.6	1.4
(MDT-TSF)$(AuI_2)_{0.436}$	0.436	4.5	1.95	2.8 (γ)	2.1	1.3
	319	121	61	4.3 (δ)	3.6	1.2
(MDT-ST)$(I_3)_{0.417}$	0.417	4.3	2.00	1.7 (γ)	2.1	0.81
	278	205	25	2.9 (δ)	3.8	0.76

where θ is the angle of the field from the conducting plane ($\parallel ab$-plane) [63]. The observed upper critical fields of (MDT-TSF)$(I_3)_{0.422}$ are well reproduced using the anisotropic 3D model (figure 16(c)). Anisotropic 3D superconductivity is characteristic of the MDT-TSF and MDT-ST superconductors and is due to the direct donor–donor interactions coming from the corrugated conducting sheet structure (figure 9(b)).

A thermodynamic study has been performed for (MDT-TSF)$(AuI_2)_{0.436}$ [64]. The electronic heat capacity coefficients have been determined; γ^* for the superconducting state and γ_N for the normal state are 6 and 9 mJ K^{-2} mol^{-1}, respectively. Although the thermodynamic T_c is 3.0 K and the present compound is a bulk superconductor, the superconducting transition is broad despite the sharp transition in the transport measurements.

The superconducting transition temperature of (MDT-TSF)$(I_3)_{0.422}$ is slightly higher than that of (MDT-TSF)$(AuI_2)_{0.436}$. For the Bardeen–Cooper–Schrieffer-type superconductors, the larger density of states and Debye temperature give the higher T_c. As shown in table 5, however, the calculated density of states, $N(E_F)$, of the I_3 salt is smaller than that of the AuI_2 salt, in disagreement with the Bardeen–Cooper–Schrieffer formula.

Although the cross-sectional area of the Fermi surface of the I_3 salt is smaller than that of the AuI_2 salt, the effective cyclotron masses of the γ and δ orbits estimated from the Shubnikov–de Haas oscillations of the I_3 salt are heavier than those of the AuI_2 salt, as shown in table 5. In κ-(ET)$_2$Cu(NCS)$_2$ and α-(ET)$_2$NH$_4$Hg(SCN)$_4$, the Shubnikov–de Haas oscillations under high pressure show that the higher T_c state has the heavier effective cyclotron mass [65, 66].

The bare cyclotron mass, m_c, is associated with the cyclotron frequency, ω_c, by

$$\omega_c = \frac{eB}{m_c}. \tag{7}$$

This mass involves an average of the dispersion relation along the periodic orbit. Equation (7) can be rearranged to give

$$m_c = \frac{\hbar^2}{2\pi}\frac{\partial A_F(E_F)}{\partial E_F}, \tag{8}$$

where $A_F(E_F)$ is the cross-sectional area of the closed Fermi surface defined using the circuit of the carrier motion in the presence of a magnetic field B [67]. The effective cyclotron mass, m^*, obtained from the quantum oscillations includes not only the band dispersion but also all interactions, i.e. electron–phonon and electron–electron interactions. Therefore, we have written the observed effective cyclotron mass as m^* to distinguish the bare cyclotron mass m_c. The effective cyclotron mass of the quasiparticle is expressed as

$$m^* = (1+\lambda_{ep})(1+\lambda_{ee})m_c, \tag{9}$$

where λ_{ep} is an electron–phonon interaction and λ_{ee} is an electron–electron interaction. Therefore, the ratio m^*/m_c denotes the magnitude of the interactions. We can estimate the ratio between the effective cyclotron mass determined using the Shubnikov–de Haas oscillations and the bare cyclotron mass estimated using equation (8) from the band calculation [68, 69]. The calculated results, m_c/m_0 and m^*/m_c, are also listed in table 5 [32]. The obtained m^*/m_c increases with increasing T_c. This tendency shows us that the mass enhancement, i.e. the strong many-body effect, is the major factor that increases T_c. A similar relation has been found between T_c and m^*/m_c for other organic superconductors, κ-(ET)$_2X$ and κ-(BETS)$_2X$ [69].

5. Metal–insulator transition and superconductivity of (MDT-TS)$(AuI_2)_{0.441}$

The noninteger composition, (MDT-TS)$(AuI_2)_{0.441}$, has been determined from the ratio of the donor lattice ($a = 3.992(3)$ Å) to the anion lattice ($a' = 9.045(6)$ Å) as $a/a' = 0.4413(3)$ [31]. This compound shows a metal–insulator transition at low temperatures. Owing to the sulfur substitution, the total bandwidth, W, of (MDT-TS)$(AuI_2)_{0.441}$ is 26% smaller than that of (MDT-ST)$(I_3)_{0.417}$ [34]. Therefore, the electronic correlation of the MDT-TS salt is the strongest among the MDT-TSF series conductors. The calculated Fermi surface of (MDT-TS)$(AuI_2)_{0.441}$ is, however, a 2D one, not markedly different from the superconducting selenium analogs.

The resistivities under various pressures are shown in figure 17 [34, 37]. At ambient pressure, the resistivity decreases with decreasing temperature and increases below $T_\rho = 85$ K, where $d(\ln R)/d(1/T)$ is zero at T_ρ. The metal–insulator transition temperature, T_{MI}, is determined

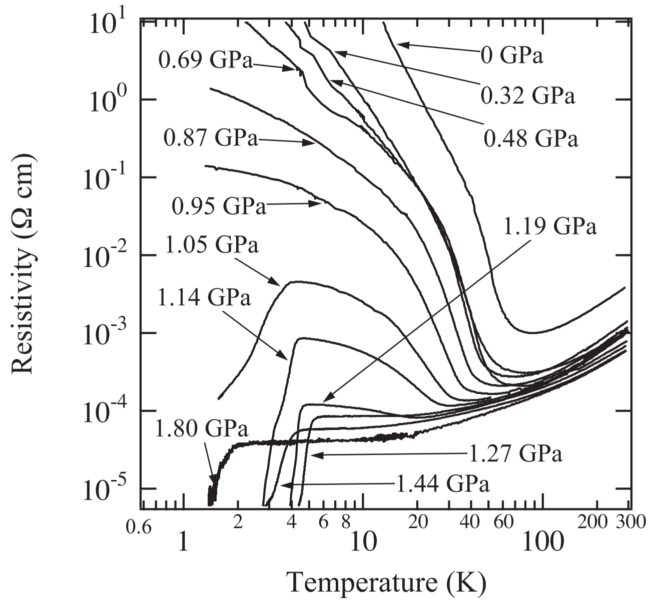

Figure 17. Temperature dependence of the resistivity under various pressures.

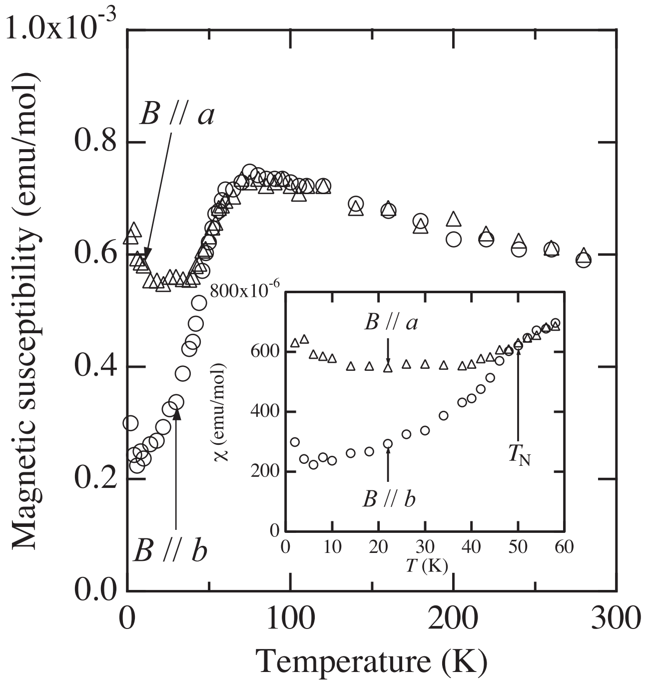

Figure 18. Temperature dependence of the static magnetic susceptibilities. The inset shows the data in the low-temperature region.

from the peak of $\mathrm{d}(\ln R)/\mathrm{d}(1/T)$ as $T_{\mathrm{MI}} = 50\,\mathrm{K}$ at ambient pressure. T_ρ and T_{MI} shift to lower temperatures as the pressure increases, and the superconducting phase appears above $P_{\mathrm{c}} = 1.05\,\mathrm{GPa}$ below onset $T_{\mathrm{c}} = 4.3\,\mathrm{K}$ (midpoint $T_{\mathrm{c}} = 3.2\,\mathrm{K}$). The resistance peak observed above 1.05 GPa corresponds to the superconducting onset T_{c}. The resistance peak is suppressed with increasing pressure, and T_{c} increases with increasing pressure. At 1.27 GPa, the resistance peak vanishes and the normal Fermi-liquid-like behavior appears. The maximum midpoint (onset) T_{c} is 4.9 K (6.2 K) at 1.27 GPa, and T_{c} decreases with $\mathrm{d}T_{\mathrm{c}}/\mathrm{d}P \sim -6\,\mathrm{K\,GPa^{-1}}$ above this pressure value.

The uniaxial strain effects of the present compound have been investigated [70]. The superconducting state appears under uniaxial strains in all directions. The superconducting critical pressure decreases in the order of $P_{\mathrm{c},\|a} > P_{\mathrm{c},\|b} > P_{\mathrm{c},\|c}$, and these are larger than the critical value of the hydrostatic pressure.

Figure 18 shows the static magnetic susceptibility (χ_a and χ_b), where we define 1 mol as $(\mathrm{MDT\text{-}TS})_{2.27}(\mathrm{AuI_2})$ [34]. Despite the decreasing resistivity at high temperatures, the spin susceptibility gradually increases with decreasing temperature, indicating a strongly correlated state. To the best of our knowledge, there is no organic conductor showing decreasing resistivity together with increasing susceptibility. Both χ_a and χ_b have a broad peak at 75 K, and decrease below this temperature. The magnetic susceptibility shows anisotropic behavior below the antiferromagnetic transition at $T_{\mathrm{N}} = 50\,\mathrm{K}$. This temperature agrees with the metal–insulator transition temperature, T_{MI}, observed in the resistivity. The easy axis corresponds to the crystallographic b-axis. The temperature at which the susceptibility has a peak is close to T_ρ, suggesting that the resistivity minimum is potentially associated with the magnetic fluctuations above T_{MI}.

The antiferromagnetism has been confirmed from the results of the magnetic torque measurements, as shown in figures 19(a) and (b) [37]. The magnetic torque curves have a peak at 6.9 T under $|\theta| = 0.7°$ in the bc-plane (figure 19(a)), coming from the spin–flop transition from the low-field antiferromagnetic state to the high-field canted antiferromagnetic state. By contrast, the magnetic torque curves do not show peak structure in the ac-plane (figure 19(b)), indicating that the ground state is a uniaxial antiferromagnetic ordered state with the easy axis parallel to the b-axis. The present compound does not show a clear signal above the spin–flop field owing to the transition from the canted antiferromagnetic state to the field-induced ferromagnetic state up to 14.5 T.

The magnetic torque, τ, for a uniaxial antiferromagnet is expressed as

$$\tau = \frac{1}{2}(\chi_\perp - \chi_\|)B^2 \frac{\sin 2\theta}{\mu_0\sqrt{\lambda^2 - 2\lambda\cos 2\theta + 1}}, \tag{10}$$

$$\lambda = \left(\frac{B}{B_{\mathrm{sf}}}\right)^2, \tag{11}$$

$$B_{\mathrm{sf}} = \sqrt{\frac{2\mu_0 K_u}{(\chi_\perp - \chi_\|)}}, \tag{12}$$

where $\chi_\|$ and $\chi_\perp$ are the spin susceptibilities parallel and perpendicular to the easy axis, respectively, θ is the angle between the applied field and the easy axis, B_{sf} is the spin–flop field, μ_0 is the vacuum magnetic permeability, and K_u is the anisotropy energy [71, 72]. The spin–flop field, $B_{\mathrm{sf}} = 6.9\,\mathrm{T}$, is obtained by fitting with these equations. The anisotropy energy is estimated as $K_u = 1.4 \times 10^{-1}\,\mathrm{J\,mol^{-1}}$ under $\chi_\| = 0$ and $\chi_\perp = 6.0 \times 10^{-4}\,\mathrm{emu\,mol^{-1}}$. The peak structure of the

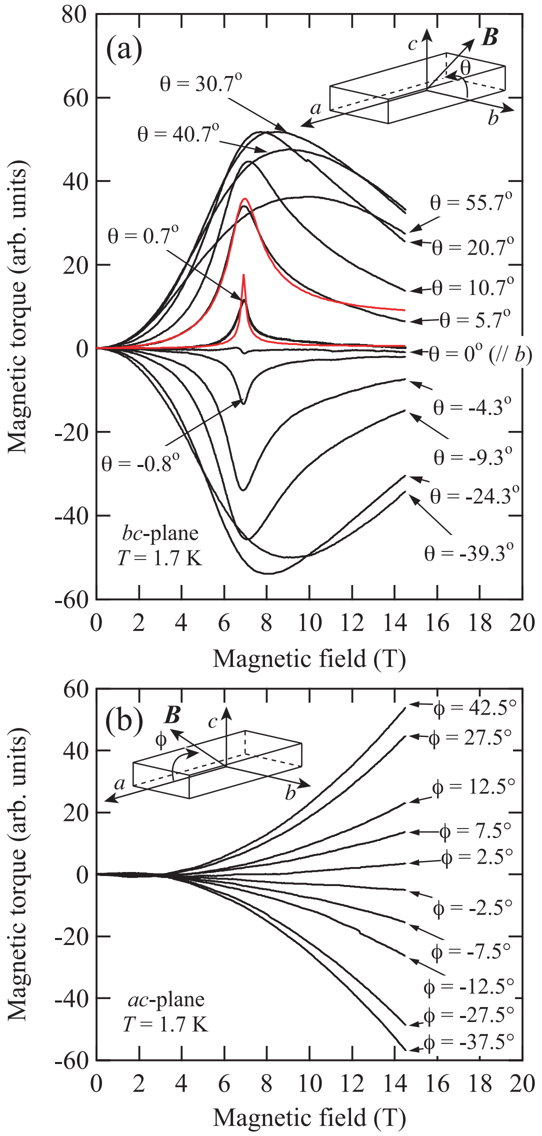

Figure 19. Magnetic torque curves of $(\mathrm{MDT\text{-}TS})(\mathrm{AuI_2})_{0.441}$ at 1.7 K under various magnetic field directions of θ and ϕ, which are the angles tilted (a) from b to c and (b) from a to c axes, respectively. The red lines in (a) are the fitted results.

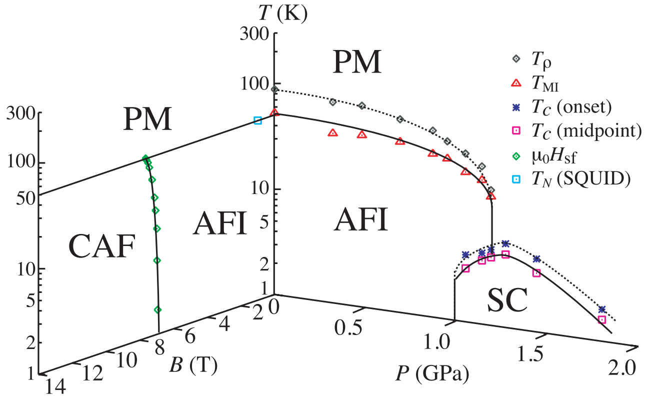

Figure 20. Phase diagram of $(\mathrm{MDT\text{-}TS})(\mathrm{AuI_2})_{0.441}$ (PM: paramagnetic metal, AFI: antiferromagnetic insulator, SC: superconductor, CAF: canted antiferromagnetic state). The solid and dotted lines are guides for the eye.

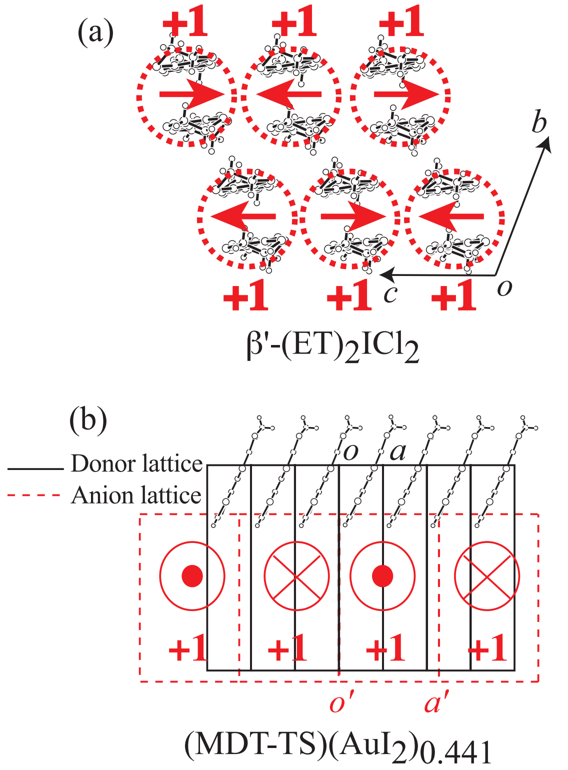

Figure 21. Model of spin arrangements for (a) β'-$(\mathrm{ET})_2\mathrm{ICl_2}$ and (b) $(\mathrm{MDT\text{-}TS})(\mathrm{AuI_2})_{0.441}$. Dotted circles in (a) represent dimers.

magnetic torque curve vanishes at 52 K, in agreement with $T_\mathrm{N} = 50$ K defined from the anisotropic behavior of the spin susceptibility.

Figure 20 shows the temperature–pressure–magnetic field phase diagram of $(\mathrm{MDT\text{-}TS})(\mathrm{AuI_2})_{0.441}$ based on the transport and magnetic measurements [37]. This is similar to the phase diagram of $(\mathrm{TM})_2X$ [73] and that of κ-$(\mathrm{ET})_2X$ [74], where TM is the general abbreviation for tetramethyltetrathiafulvalene (TMTTF) and TMTSF. It seems that the superconducting phase exists under the insulating phase at approximately 1.1 GPa in figure 20. This relationship between the superconducting and insulating phases is the same as those of κ-$(\mathrm{ET})_2\mathrm{Cu[N(CN)_2]Cl}$ [75], β'-$(\mathrm{ET})_2\mathrm{ICl_2}$ [76], and $(\mathrm{TMTSF})_2\mathrm{AsF_6}$ [77].

The magnetic insulating state below $T_\mathrm{N} = 50$ K is not a simple antiferromagnetic state with alternate spins like β'-$(\mathrm{ET})_2\mathrm{ICl_2}$, as shown in figure 21(a), because each molecule or dimer does not have one carrier. In this sense, the insulating state is regarded as a kind of spin-density-wave state. In contrast to $(\mathrm{TM})_2X$, however, the electronic state of the present compound is two-dimensional, and the Fermi surface does not nest. This new electronic state is simply understood by assuming a localized state that is incommensurate to the donor sites. One of the possible carrier and spin arrangements is shown in figure 21(b), where the unit of 2.27 ($= 1/0.441$) donor molecules has one carrier and spin; this is commensurate to the anion lattice [34].

Yoshioka *et al* [78] have shown the possibility of the metal–insulator transition in organic conductors with noninteger carrier number based on the one-dimensional

Table 6. Néel temperature T_N, spin–flop field B_{sf}, anisotropy energy K_u, maximum midpoint superconducting transition temperature T_c^{max} under pressure P, energy band filling, and ground state (AFI: antiferromagnetic insulator; AF Mott: antiferromagnetic Mott insulator; IC-SDW: incommensurate spin-density-wave state; C-SDW: commensurate spin-density-wave state) for (MDT-TS)$(AuI_2)_{0.441}$ [37], β'-$(ET)_2ICl_2$ [76, 80], $(TMTSF)_2AsF_6$ [77, 81], and $(TMTTF)_2Br$ [82, 83].

	(MDT-TS)$(AuI_2)_{0.441}$	β'-$(ET)_2ICl_2$	$(TMTSF)_2AsF_6$	$(TMTTF)_2Br$
T_N(K)	50	22	12	13
B_{sf}(T)	6.9	1.1	0.45	0.42
K_u(J/mol)	1.4×10^{-1}	5.4×10^{-3}	1.5×10^{-4}	–
T_c^{max}(K)	4.9	13.4	1.26[a]	0.8
P (GPa)	1.27	8.2	1.2	2.6
Band filling	0.7794(2)	Effective 0.5	0.75	0.75
Ground state	AFI	AF Mott	IC-SDW	C-SDW

[a] T_c is defined as the intersection of the extrapolated normal resistivity curve with the tangent drawn through the inflexion point in [77].

extended Hubbard model, where donor carriers slightly deviate from 3/4-filling, under an incommensurate periodic potential from anions. They have pointed out that the *incommensurate Mott insulator* can be generated using the anion potential and the ratio between the on-site Coulomb repulsion and the nearest-neighbor transfer integral without the nearest-neighbor Coulomb repulsion. Seo *et al* [79] have found an antiferromagnetic insulating state as a mean-field solution in the two-dimensional model for (MDT-TS)$(AuI_2)_{0.441}$. The solution shows that the charge disproportionation occurs owing to the incommensurate anion potential, and the period of the spin arrangement matches the anion periodicity. They note that the present insulating state should be distinguished from the charge ordering observed in 3/4-filled systems, which is accompanied with symmetry breaking in the charge degree of freedom. In their results, the charge disproportionation occurs even in the paramagnetic metallic state owing to the incommensurate anion potential, and the metal–insulator transition has no symmetry breaking in the charge degree of freedom.

Table 6 lists the characteristic parameters of (MDT-TS)$(AuI_2)_{0.441}$ [37], β'-$(ET)_2ICl_2$ [76, 80] $(TMTSF)_2AsF_6$ [77, 81] and $(TMTTF)_2Br$ [82, 83]. The latter three compounds show three types of antiferromagnetic ordered states, antiferromagnetic Mott insulating state, incommensurate spin-density-wave state and commensurate spin-density-wave state. The TMTSF and TMTTF salts have almost the same antiferromagnetic parameters and superconducting transition temperatures. By contrast, β'-$(ET)_2ICl_2$ has much larger parameters than $(TM)_2X$. This indicates some relationship between the antiferromagnetic parameters and T_c. Although all antiferromagnetic parameters of (MDT-TS)$(AuI_2)_{0.441}$ are much larger than those of the other compounds listed in table 6, the highest T_c is much lower than that of β'-$(ET)_2ICl_2$.

There are two important differences between the MDT-TS and β'-ET superconductors listed in table 6. The first one is the energy band filling. The β'-ET salt has an effective half-filled band because of its strong dimerized structure. By contrast, the band filling of the MDT-TS salt is 0.7794(2). The electronic correlation of the β'-ET salt should be stronger than that of the MDT-TS salt. In the layered organic superconductors, the κ-type ET superconductors and MDT-TSF ones show that the strength of the many-body effect is the major determinant of T_c [32, 69]. Therefore, the difference in the band filling is a possible reason for the difference in T_c. The second point is the incommensurate anion potential. The relationship between the incommensurate potential and the appearance of the superconducting phase is unknown. However, the present results suggest that the incommensurate potential suppresses the superconducting phase.

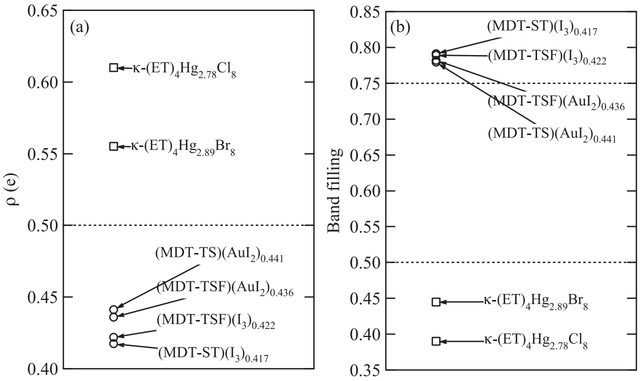

Figure 22. Charge transfer degree (a) and effective energy band filling (b) of the incommensurate organic superconductors.

6. Summary and outlook

The charge transfer degree, ρ, of the incommensurate organic superconductors is shown in figure 22(a). The present values of ρ of κ-$(ET)_4Hg_{3-\delta}X_8$ are calculated by assuming $(Hg^{2+})_{3-\delta}(X^-)_8$. Although ρ of the MDT-TSF series salts is smaller than 0.5 of the usual D_2A salts, ρ of κ-$(ET)_4Hg_{3-\delta}X_8$ is larger than 0.5. The κ-type arrangement has a strong dimerized structure, then κ-$(ET)_4Hg_{3-\delta}X_8$ has a nearly effective half-filled band system, i.e. the doped Mott insulator. By contrast, the MDT-TSF series salts have a nearly 3/4-filled band system, as shown in figure 22(b).

Many physical properties of κ-$(ET)_4Hg_{3-\delta}X_8$ have been reported [38, 84–91]. The thermodynamic superconducting transition of κ-$(ET)_4Hg_{2.89}Br_8$ is broad, similar to that of (MDT-TSF)$(AuI_2)_{0.436}$, which suggests that the broad phase transition is characteristic behavior of the incommensurate superconductors [89]. High-pressure resistance measurements of κ-(ET)$_4$Hg$_{3-\delta}$X$_8$ show the pressure-induced insulating phase at low temperature above 3.0 GPa for the $X = \mathrm{Br}$ salt [86] and 5.0 GPa for the $X = \mathrm{Cl}$ salt [91]. However, it is not clear whether this insulating phase originated in the incommensurate potential. In this regard, a resistance measurement under extremely high pressure should be carried out for the MDT-TSF series superconductors. By contrast, the Fermi surface reconstruction observed for both (MDT-TSF)(AuI$_2$)$_{0.436}$ and (MDT-ST)(I$_3$)$_{0.417}$ is a clear new phenomenon certainly caused by the *incommensurate lattice potential*.

The mechanism of the metal–insulator transition of (MDT-TS)(AuI$_2$)$_{0.441}$ is important, because there is a possibility of a new type of insulating state, i.e. the *incommensurate Mott insulator*. The present experimental results do not provide any information on the microscopic magnetic structure, i.e. the periodicity of the spin arrangement. Therefore, the mechanism of the metal–insulator transition of the present compound is unclear. Neutron diffraction, x-ray magnetic diffraction, and NMR measurements are potential tools to clarify the mechanism.

Recently, nonlinear transport properties have been investigated for an incommensurate organic conductor (MDT-TS)I$_{0.85}$Br$_{0.41}$, and this compound shows *current* oscillations under dc voltage, the thyristor effect, in the antiferromagnetic insulating phase [92]. By contrast, an inorganic compound, Ba$_2$NaNb$_5$O$_{15}$, called BSN, shows self-generated *voltage* oscillations under dc current below 873 K, and this oscillation becomes chaotic at approximately 773 K [93, 94]. The voltage oscillation phenomenon does not appear in the structural-incommensurate phase (ferroelastic and ferroelectric) existing below the ferroelastic phase transition temperature $T_{\mathrm{I}} \sim 573$ K. Therefore, the role of the incommensurate potential is unclear in the organic thyristor.

The MDT-TSF series superconductors have extended the frontier of *incommensurate composite crystals* among organic superconductors. We hope that new physical phenomena based on the incommensurate potential will be discovered.

Acknowledgments

We are grateful to the coauthors of our own works cited in the references, particularly Professors T Mori, T Otsubo and Dr S Uji for valuable discussion in our collaborative studies, and for many valuable comments on this review.

References

[1] Williams J M, Ferraro J R, Thorn R J, Carlson K D, Geiser U, Wang H H, Kini A M and Whangbo M-H 1992 *Organic Superconductors (Including Fullerenes)* (Englewood Cliffs, NJ: Prentice-Hall)

[2] Ishiguro T, Yamaji K and Saito G 1998 *Organic Superconductors* 2nd edn (Berlin: Springer)

[3] Toyota N, Lang M and Müller J 2007 *Low-Dimensional Molecular Metals* (Berlin: Springer)

[4] Kumai R, Asamitsu A and Tokura Y 1998 *J. Am. Chem. Soc.* **120** 8263

[5] Katsuhara M, Kimura S, Mori T, Misaki Y and Tanaka K 2002 *Chem. Mater.* **14** 458

[6] Mori H, Kamiya M, Haemori M, Suzuki H, Tanaka S, Nishio Y, Kajita K and Moriyama H 2002 *J. Am. Chem. Soc.* **124** 1251

[7] Yamamoto H M and Kato R 2000 *Chem. Lett.* **29** 970

[8] Mori T 2004 *Chem. Rev.* **104** 4947

[9] Lyubovskaya R N, Lyubovskiĭ R B, Shibaeva R P, Aldoshina M Z, Gol'denberg L M, Rozenberg L P, Khidekel' M L and Shul'pyakov Y F 1985 *JETP Lett.* **42** 468

[10] Lyubovskaya R N, Zhilyaeva E I, Pesotskiĭ S I, Lyubovskiĭ R B, Atovmyan L O, D'yachenko O A and Takhirov T G 1987 *JETP Lett.* **46** 188

[11] Takimiya K, Kataoka Y, Aso Y, Otsubo T, Fukuoka H and Yamanaka S 2001 *Angew. Chem., Int. Ed. Engl.* **40** 1122

[12] Cummins H Z 1990 *Phys. Rep.* **185** 211

[13] van Smaalen S 2007 *Incommensurate Crystallography* (New York: Oxford University Press)

[14] Petricek V, Maly K, Coppens P, Bu X, Cisarova I and Frost-Jensen A 1991 *Acta Crystallogr.* A **47** 210

[15] Schukat G and Fanghänel E 1996 *Sulfur Rep.* **18** 1

[16] Ogura F and Takimiya K 1999 *in Organoselenium Chemistry* ed T G Back (Oxford: Oxford University Press) p 257

[17] Jérome D, Mazaud A, Ribault M and Bechgaard K 1980 *J. Physique Lett.* **41** L95

[18] Kobayashi H, Kobayashi A and Cassoux P 2000 *Chem. Soc. Rev.* **29** 325

[19] Papavassiliou G C, Mousdis G A, Zambounis J S, Terzis A, Hountas A, Hilti B, Mayer C W and Pfeiffer J 1988 *Synth. Met.* **27** B379

[20] Kini A M *et al* 1989 *Solid State Commun.* **69** 503

[21] Morikami A, Takimiya K, Aso Y and Otsubo T 1999 *Org. Lett.* **1** 23

[22] Takimiya K, Morikami A and Otsubo T 1997 *Synlett* **1997** 319

[23] Jigami T, Takimiya K, Otsubo T and Aso Y 1998 *J. Org. Chem.* **63** 8865

[24] Takimiya K, Oharuda A, Morikami A, Aso Y and Otsubo T 2000 *Eur. J. Org. Chem.* **2000** 3013

[25] Brandsma L, Wijers H E and Jonker M C 1963 *Rec. Trav. Chim.* **82** 208

[26] Takimiya K, Kataoka Y, Niihara N, Aso Y and Otsubo T 2003 *J. Org. Chem.* **68** 5217

[27] Hiskey R G and Carroll F I 1961 *J. Am. Chem. Soc.* **83** 4644

[28] Kawamoto T, Mori T, Takimiya K, Kataoka Y, Aso Y and Otsubo T 2002 *Phys. Rev.* B **65** 140508

[29] Takimiya K, Kodani M, Kataoka Y, Aso Y, Otsubo T, Kawamoto T and Mori T 2003 *Chem. Mater.* **15** 3250

[30] Takimiya K, Takamori A, Aso Y, Otsubo T, Kawamoto T and Mori T 2003 *Chem. Mater.* **15** 1225

[31] Takimiya K, Kodani M, Niihara N, Aso Y, Otsubo T, Bando Y, Kawamoto T and Mori T 2004 *Chem. Mater.* **16** 5120

[32] Kawamoto T, Mori T, Konoike T, Enomoto K, Terashima T, Uji S, Kitagawa H, Takimiya K and Otsubo T 2006 *Phys. Rev.* B **73** 094513

[33] Kawamoto T, Mori T, Uji S, Yamaura J, Kitagawa H, Takamori A, Takimiya K and Otsubo T 2005 *Phys. Rev.* B **71** 172503

[34] Kawamoto T, Bando Y, Mori T, Takimiya K and Otsubo T 2005 *Phys Rev.* B **71** 052501

[35] Kodani M, Takamori A, Takimiya K, Aso Y and Otsubo T 2002 *J. Solid State Chem.* **68** 582

[36] Papavassiliou G C, Mousdis G A, Yiannopoulos S Y and Zambounis J S 1988 *Synth. Met.* **27** B373

[37] Kawamoto T, Bando Y, Mori T, Konoike T, Takahide Y, Terashima T, Uji S, Takimiya K and Otsubo T 2008 *Phys. Rev.* B **77** 224506

[38] Li R, Petricek V, Yang G, Coppens P and Naughton M 1998 *Chem. Mater.* **10** 1521

[39] Marks T J and Kalina D W 1983 *Extended Linear Chain Compounds* vol I ed J S Miller (New York: Plenum) chapter 6

[40] Cowie M *et al* 1979 *J. Am. Chem. Soc.* **101** 2921

[41] Zambounis J S, Patsis A P, Kamitsos E I, Mayer C W and Papavassiliou G C 1995 *J. Raman Spectrosc.* **26** 9

[42] Cisarova I, Maly K, Bu X, Frost-Jensen A, Sommer-Larsen P and Coppens P 1991 *Chem. Mater.* **3** 647

[43] Coppens P 1995 *Acta Crystallogr.* B **51** 402

[44] Mori T, Kobayashi A, Sasaki Y, Kobayashi H, Saito G and Inokuchi H 1984 *Bull. Chem. Soc. Japan* **57** 627

[45] Whangbo M-H, Walsh W M Jr, Haddon R C and Wudl F 1982 *Solid State Commun.* **43** 637

[46] Mori T and Katsuhara M 2002 *J. Phys. Soc. Japan* **71** 826

[47] Kawamoto T, Mori T, Terakura C, Terashima T, Uji S, Takimiya K, Aso Y and Otsubo T 2003 *Phys. Rev.* B **67** 020508

[48] Kawamoto T, Mori T, Terakura C, Terashima T, Uji S, Tajima H, Takimiya K, Aso Y and Otsubo T 2003 *Eur. Phys. J.* B **36** 161

[49] Kawamoto T, Mori T, Enomoto K, Konoike T, Terashima T, Uji S, Takamori A, Takimiya K and Otsubo T 2006 *Phys. Rev.* B **73** 024503

[50] Koster G F 1957 *Solid State Phys.* **5** 173

[51] Jacobsen C S 1988 *Semiconductors and Semimetals* vol 27 ed E Conwell (Tokyo: Academic) chapter 5

[52] Shoenberg D 1984 *Magnetic Oscillations in Metals* (Cambridge: Cambridge Universisty Press)

[53] Wosnitza J 1996 *Fermi Surfaces of Low Dimensional Organic Metals and Superconductors* (Berlin: Springer)

[54] Azbel M Y 1979 *Phys. Rev. Lett.* **43** 1954

[55] Hill S *et al* 1997 *Phys. Rev.* B **55** 2018

[56] Everson M P, Johnson A, Lu H-A, Coleman R V and Falicov L M 1987 *Phys. Rev.* B **36** 6953

[57] Razavi F S, Datars W R, Chartier D and Gillespie R J 1979 *Phys. Rev. Lett.* **42** 1182

[58] Batalla E, Razavi F S and Datars W R 1982 *Phys. Rev.* B **25** 2109

[59] Hanasaki N, Kagoshima S, Hasegawa T, Osada T and Miura N 1998 *Phys. Rev.* B **57** 1336

[60] Yagi R and Iye Y 1994 *Solid State Commun.* **89** 275

[61] Hussey N E, Abdel-Jawad M, Carrington A, Mackenzie A P and Balicas L 2003 *Nature* **425** 814

[62] Kawamoto T, Mori T, Terashima T, Uji S, Takamori A, Takimiya K and Otsubo T 2005 *J. Phys. Soc. Japan* **74** 1529

[63] Tinkham M 1996 *Introduction to Superconductivity* 2nd edn (New York: McGraw-Hill)

[64] Ishikawa T, Nakazawa Y, Yamashita S, Oguni M, Saito K, Takimiya K and Otsubo T 2006 *J. Phys. Soc. Japan* **75** 074606

[65] Caulfield J, Lubczynski W, Pratt F L, Singleton J, Ko D Y K, Hayes W, Kurmoo M and Day P 1994 *J. Phys. Condens. Matter* **6** 2911

[66] Brooks J S *et al* 1995 *Phys. Rev.* B **52** 14457

[67] Ziman J M 1972 *Principles of the Theory of Solids* 2nd edn (Cambridge: Cambridge University Press)

[68] Merino J and McKenzie R H 2000 *Phys. Rev.* B **62** 2416

[69] Kawamoto T and Mori T 2006 *Phys. Rev.* B **74** 212502

[70] Bando Y, Kawamoto T, Mori T, Takimiya K and Otsubo T 2008 *J. Phys. Soc. Japan* **77** 014706

[71] Yosida K 1951 *Prog. Theor. Phys.* **6** 691

[72] Nagamiya T, Yosida K and Kubo R 1955 *Adv. Phys.* **4** 1

[73] Jérome D 1991 *Science* **252** 1509

[74] Kanoda K 1997 *Hyperfine Interact.* **104** 235

[75] Lefebvre S, Wzietek P, Brown S, Bourbonnais C, Jérome D, Mézière C, Fourmigué M and Batail P 2000 *Phys. Rev. Lett.* **85** 5420

[76] Taniguchi H, Miyashita M, Uchiyama K, Satoh K, Môri N, Okamoto H, Miyagawa K, Kanoda K, Hedo M and Uwatoko Y 2003 *J. Phys. Soc. Japan* **72** 468

[77] Brusetti R, Ribault M, Jérome D and Bechgaard K 1982 *J. Physique* **43** 801

[78] Yoshioka H, Seo H and Fukuyama H 2005 *J. Phys. Soc. Japan* **74** 1922

[79] Seo H, Yoshioka H and Otsuka Y 2008 *J. Phys.: Conf. Ser.* **132** 012018

[80] Yoneyama N, Miyazaki A, Enoki T and Saito G 1999 *Bull. Chem. Soc. Japan* **72** 639

[81] Mortensen K, Tomkiewicz Y and Bechgaard K 1982 *Phys. Rev.* B **25** 3319

[82] Parkin S S P, Scott J C, Torrance J B and Engler E M 1982 *Phys. Rev.* B **26** 6319

[83] Balicas L, Behnia K, Kang W, Canadell E, Auban-Senzier P, Jérome D, Ribault M and Fabre J M 1994 *J. Physique* I **4** 1539

[84] Sekretarczyk G, Graja A, Pichet J, Lyubovskaya R N and Lyubovskii R B 1988 *J. Physique* **49** 653

[85] Schirber J E, Overmyer D L, Venturini E L, Wang H H, Carlson K D, Kwok W K, Kleinjan S and Williams J M 1989 *Physica* C **161** 412

[86] Bud'ko S L, Gapotchenko A G, Luppov A E, Lyubovskaya R N and Lyubovskii R B 1992 *Sov. Phys.—JETP* **74** 983

[87] Lyubovskii R B, Lyubovskaya R N and Dyachenko O A 1996 *J. Physique* I **6** 1609

[88] Ohmichi E, Ishiguro T, Sakon T, Sasaki T, Motokawa M, Lyubovskii R B and Lyubovskaya R N 1999 *J. Supercond.* **12** 505

[89] Naito A, Nakazawa Y, Saito K, Taniguchi H, Kanoda K and Sorai M 2005 *Phys. Rev.* B **71** 054514

[90] Taniguchi H, Okuhata T, Nagai T, Satoh K, Môri N, Shimizu Y, Hedo M and Uwatoko Y 2007 *J. Phys. Soc. Japan* **76** 113709

[91] Taniguchi H, Okuhata T, Nagai T, Miyashita M, Uchiyama K, Satoh K, Môri N, Hedo M and Uwatoko Y 2007 *J. Phys. Soc. Japan* **76** (Suppl A) 168

[92] Mori T, Bando Y, Kawamoto T, Terasaki I, Takimiya K and Otsubo T 2008 *Phys. Rev. Lett.* **100** 037001

[93] Martin S, Leber H and Martienssen W 1984 *Phys. Rev. Lett.* **53** 303

[94] Martin S and Martienssen W 1986 *Phys. Rev. Lett.* **56** 1522